The Astrophysical Journal, 923:198 (26pp), 2021 December 20 https://doi.org/10.3847/1538-4357/ac2d25

Surveying the Giant H II Regions of the Milky Way with SOFIA. III. W49A

James M. De Buizer[1], Wanggi Lim[1], Mengyao Liu[2], Nicole Karnath[1], and James T. Radomski[1]
[1] SOFIA-USRA, NASA Ames Research Center, MS 232-12, Moffett Field, CA 94035, USA; jdebuizer@sofia.usra.edu
[2] Department of Astronomy, University of Virginia, Charlottesville, VA 22904, USA
Received 2021 July 5; revised 2021 September 13; accepted 2021 October 4; published 2021 December 22

Abstract

We present our third set of results from our mid-infrared imaging survey of Milky Way Giant H II regions with our detailed analysis of W49A, one of the most distant, yet most luminous, GH II regions in the Galaxy. We used the FORCAST instrument on the Stratospheric Observatory For Infrared Astronomy (SOFIA) to obtain 20 and 37 μm images of the entire $\sim 5\farcm0 \times 3\farcm5$ infrared-emitting area of W49A at a spatial resolution of $\sim 3''$. Utilizing these SOFIA data in conjunction with previous multiwavelength observations from the near-infrared to radio, including Spitzer-IRAC and Herschel-PACS archival data, we investigate the physical nature of individual infrared sources and subcomponents within W49A. For individual compact sources, we used the multiwavelength photometry data to construct spectral energy distributions (SEDs) and fit them with massive young stellar object (MYSO) SED models and find 22 sources that are likely to be MYSOs. Ten new sources are identified for the first time in this work. Even at 37 μm we are unable to detect infrared emission from the sources on the western side of the extremely extinguished ring of compact radio emission sources known as the Welch Ring. Utilizing multiwavelength data, we derived luminosity-to-mass ratio and virial parameters of the extended radio subregions of W49A to estimate their relative ages and find that overall the subcomponents of W49A have a very small spread in evolutionary state compared to our previously studied GH II regions.

Unified Astronomy Thesaurus concepts: Infrared sources (694); Infrared sources (793); Star formation (1569); Star forming regions (1565)

1. Introduction

It is believed that the vast majority of all stars in a galaxy form within OB clusters (Lada & Lada 2003). Galactic giant H II (GH II) regions are hosts to the largest and most massive star-forming clusters in the Milky Way and thus have been used as laboratories for the study of the extreme environments of the earliest stages of clustered massive star formation (e.g., Smith et al. 1978; Conti & Crowther 2004; Moisés et al. 2011). An overview of the nature of GH II regions and why they are important to study is highlighted in detail in the introduction of Lim & De Buizer (2019, hereafter "Paper I"), which focused on the infrared properties of the GH II region W51A. That was followed up by a paper dedicated to the study of the GH II region M17 (Lim et al. 2020; hereafter "Paper II"). Building off those studies, this is the third paper in our continuing series concentrating on the study of the infrared properties of Galactic GH II regions utilizing new data obtained from the Stratospheric Observatory For Infrared Astronomy (SOFIA), this time focusing on the well-known source W49A.

Even though W49A is located on the far side of our Galaxy at a distance of 11.1 kpc (Zhang et al. 2013), it has an infrared-emitting region subtending more than $4'$ ($\sim$13 pc) on a side. This makes W49A one of the largest and most luminous ($M \sim 10^6\,M_\odot$, $L > 10^7\,L_\odot$: Becklin et al. 1973; Ward-Thompson & Robson 1990) GH II regions in the Galaxy. Given its nature as a massive star-forming region, observations toward the massive young stellar objects (MYSOs) it contains are subject to a large amount of local extinction. Additionally, due to its location in the plane of the Galaxy and its large distance, it is observed through the obscuring gas and dust of the Milky Way's Sagittarius spiral arm, which crosses the line of sight to W49A twice (Plume et al. 2004). The combined level of local and galactic extinction (estimates are as high as $A_V \sim 300$ mag; Westbrook et al. 1976) means that even at near- and mid-infrared wavelengths there is considerable obscuration. Given its significant brightness at longer wavelengths, however, W49A has been the subject of numerous studies from the infrared to radio wavelengths. A consequence of the large distance to W49A is that, unlike the previously studied GH II regions from this project, the physical scales we are probing will be much larger ($\theta_{\rm resolution} \sim 3\farcs1 \sim 35{,}000$ au). While more than 50 O-star candidates have been identified in the central region ($r \sim 45''$) of W49A alone (Alves & Homeier 2003), it is believed to harbor one of the largest concentrations of compact H II (CH II) and ultracompact H II (UCH II) regions (Welch et al. 1987), signifying that it may be a relatively young GH II region.

In Section 2, we will discuss the new SOFIA observations and give information on the data obtained. In Section 3, we will give more background on W49A as we compare our new data to previous observations and discuss individual sources and regions in depth. In Section 4, we will discuss our data analysis, modeling, and derivation of physical parameters of sources and regions. Our results and conclusions are summarized in Section 5.

2. Observations and Data Reduction

The observational techniques and reduction processes employed on the data were, for the most part, identical to those described in Paper I for W51A. Below we will highlight some of the observation and reduction details specific to these new observations. For a more in-depth discussion of these details and techniques, refer to Paper I.

All observations were made with the airborne astronomical observatory, SOFIA (Young et al. 2012), utilizing the FORCAST instrument (Herter et al. 2013). All data were

taken of W49A on the night of 2015 September 16 (Flight 239). All observations were taken at an altitude of 41,000 ft, which typically yields precipitable water vapor overburdens of less than 8 μm. FORCAST is a facility imager and spectrograph that employs a Si:As 256 × 256 blocked-impurity band (BIB) detector array to cover a wavelength range of 5–25 μm and a Si:Sb 256 × 256 BIB array to cover the range from 25 to 40 μm. Imaging data were obtained in the 20 μm ($\lambda_{\rm eff} = 19.7$ μm; $\Delta\lambda = 5.5$ μm) and 37 μm ($\lambda_{\rm eff} = 37.1$ μm; $\Delta\lambda = 3.3$ μm) filters simultaneously using an internal dichroic. In imaging mode the arrays cover a $3\farcm40 \times 3\farcm20$ instantaneous field of view with a pixel scale of $0\farcs768$ pixel^{-1} after distortion correction.

All images were obtained by employing the standard chop-nod observing technique used in ground-based thermal infrared observing, with chop throws of $4\farcm2$ and nod throws of $15'$, which were sufficiently large enough to sample clear off-source sky regions uncontaminated by the extended emission of W49A. The mid-infrared-emitting area of W49A is much larger than the FORCAST field of view and thus had to be mapped using multiple pointings. We created a mosaic from three individual pointings, with each pointing having an average on-source exposure time of about 180 s at both 20 and 37 μm. Final mosaicked images made from the individual pointing images were stitched together using the SOFIA Data Pipeline software REDUX (Clarke et al. 2015).

SOFIA data were calibrated by the SOFIA pipeline with a system of stellar calibrators taken across all flights in the flight series and applied to all targets within that flight series (see also the FORCAST calibration paper by Herter et al. 2013). Corrections are made for the airmass of the science data as well.

In order to try to resolve sources in crowded regions, the SOFIA images at 20 and 37 μm were deconvolved using the maximum likelihood method (Richardson 1972; Lucy 1974). Like all deconvolution methods, knowledge of the point-spread function (PSF) of an unresolved source is needed at each wavelength, and with a high signal-to-noise ratio (S/N). The PSF of SOFIA is slightly variable from flight to flight and observations to observation, so using a bright, isolated point source in the W49A mosaic would be most accurate. However, no such point source is present in our data. Therefore, using standard stars observed throughout several flights, an average FWHM for each wavelength was determined. Then, artificially generated PSFs (an Airy pattern calculated from the wavelength, telescope diameter, and central obscuration diameter) were constructed and convolved with a Gaussian to achieve PSFs with FWHMs that equaled the measured average FWHMs of the standard stars. These idealized PSFs were then used in the deconvolution procedure. The deconvolution routine was stopped at 100 iterations for both the 20 and 37 μm images. Deconvolutions with the average PSF from the standard star observations were also tried, and yielded nearly identical results. The deconvolved images using the idealized PSF also compared favorably to simple unsharp masking of the original images, and thus the substructures revealed in the deconvolved images are believed to be reliable. Reliable flux conservation for deconvolved data requires flat and/or zero-mean backgrounds. However, the data for W49A are pervaded by diffuse and extensive nebular dust emission, and this makes the derived fluxes of the embedded compact sources from the deconvolved data less reliable than from the natural resolution data. Therefore, the deconvolved data are only used in this study for morphological comparisons to data at other wavelengths with higher spatial resolution.

In addition to the SOFIA data, we also utilize science-ready imaging data from the Spitzer Space Telescope and Herschel Space Telescope archives. In addition to having access to the Very Large Array (VLA) 3.6 cm data with $\sim0\farcs8$ spatial resolution used in De Pree et al. (1997), we additionally obtained VLA archival data at 3.6 cm with a spatial resolution of $9\farcs8$ and a field of view of $2\farcm5$ centered on W49A.

3. Comparing SOFIA Images of W49A to Previous Imaging Observations

W49 was first discovered as a radio continuum region by Westerhout (1958) at 22 cm and consists of the high-mass star-forming region W49A and the nearby ($\sim12'$ away) supernova remnant W49B. The GH II region of W49A displays extensive extended radio continuum emission ($d \gtrsim 2'$), while at the same it is believed to harbor the highest concentration of compact and ultracompact H II regions in the Galaxy (18; Urquhart et al. 2013), with a central group of UCH II regions distributed in a ring-like structure (Welch et al. 1987). In addition to these UCH II regions, the entire region around W49A ($r \sim 8$ pc) has more than 250 massive O-type stars (Homeier & Alves 2005).

The infrared observations from SOFIA show the region to have structured but extended dust emission spread over an approximately $4' \times 3'$ area (Figure 1), which corresponds generally to the extent of the centimeter radio continuum emission seen by De Pree et al. (1997), as can be seen in Figure 2(a). While most of the infrared features are seen at both SOFIA wavelengths, the dust is more pronounced and extended at 37 μm compared to 20 μm (Figure 2), indicative of widespread cool dust.

3.1. Discussion of Individual Sources in W49A

From the first observations at arcminute resolution (Mezger et al. 1967), the radio continuum structure of W49A was seen to display two intensity peaks separated by $\sim2\farcm5$. Multiple monikers were used in naming these sources in early observations; however, they are now most often denoted W49 North and W49 South, or W49N and W49S (e.g., Dreher et al. 1984). Dickel & Goss (1990) observed the radio continuum emission at $2''$ resolution with the VLA and labeled the peaks in emission they found as A through S by increasing R.A. W49A was revisited with the VLA by De Pree et al. (1997), and even more radio continuum emission peaks were found. Those newly detected peaks that were resolved from or close to already known peaks were indexed with a number (e.g., G_1, G_2, etc.); however, entirely new peaks independent of already known sources were labeled with a double letter (e.g., AA, BB, etc.), in order of increasing R.A. Even higher spatial resolution observations by De Pree et al. (2000, 2020) at 3.6 cm ($\theta_{\rm beam} \sim 0\farcs15$) and at several-millimeter wavelengths ($0\farcs04 < \theta_{\rm beam} < 0\farcs35$) further resolved details and even more subsources in the crowded southwestern side of the Welch Ring (i.e., sources A through H).

The subregion containing sources Q, R, and S are also occasionally referred to by the collective moniker of W49 Southwest, first named as such by Webster et al. (1971). Figure 2 shows the SOFIA observations at 20 and 37 μm of W49A, with the main regions labeled (i.e., Central W49A,

Figure 1. A three-color image of a $\sim 5' \times 4'$ field centered on W49A. Blue is the SOFIA-FORCAST 20 μm data, green is the SOFIA-FORCAST 37 μm data, and red is the Herschel-PACS 70 μm data. Overlaid in white is the Spitzer-IRAC 3.6 μm data, which traces the revealed stars within W49A, field stars, and hot dust.

W49 South, and W49 Southwest), as well as all of the sources that are distributed outside of these main regions.

While discussing the nature of the individual sources below, we will sometimes refer to the results of our spectral energy distribution (SED) model fitting (like derived luminosity, for instance), which are discussed in depth in Section 4. See that section for further information describing the SED model-fitting algorithm used, as well as details regarding the assumptions, limitations, and results of the SED fitting.

3.1.1. W49 South

W49 South is the brightest source in all of W49A in the infrared from ~ 3 μm out to ~ 20 μm. It is saturated in all Spitzer-IRAC and MIPS wavelengths, except in IRAC channels 1 and 2 (3.6 and 4.5 μm). In our 37 μm data and at longer wavelengths seen by Herschel, it becomes the second brightest peak to source G.

Smith et al. (2000) claim that there is a roughly circular halo of extended emission in their data at wavelengths from 8.0 to 20 μm and suggest the emission may be tracing a nearly complete 4″ radius dust shell. However, our 37 μm data show what appears to be a lane of lesser emission running NW–SE through the extended emission just east of the peak (Figure 3). Smith et al. (2000) discuss a protrusion to the northwest in their 20 μm data; however, it is likely that this is an artifact of this darker lane creating a notch in the extended emission on the northern part of the source, and because the western side is brighter it looks like a protrusion.

The radio continuum emission from this source is classified as a "cometary" shape (De Pree et al. 1997), with a bright arc-shaped ridge of emission and a diffuse tail of emission toward the southeast. Overall, the infrared emission looks similar to the radio at wavelengths from 3.6 μm through the mid-infrared (Smith et al. 2000), and out to the longest wavelengths we see with SOFIA at 37 μm (Figure 4), but with some distinctions discussed below.

The large-scale extended emission at 37 μm (and at Herschel 70 μm) reaches almost an arcminute to the east of the peak and is pervaded by centimeter continuum emission (see Figure 4) as seen by De Pree et al. (1997). In our 20 μm image and in the Spitzer wavelengths, the extended emission of W49 South is elongated more toward the southeast (at a p.a. of $\sim 135°$), but the primary extension of emission at 37 and 70 μm is more toward the northeast (at a p.a. of $\sim 75°$). Because radio continuum emission is coming from the regions covered by both the 20 and 37 μm extended emission, this implies variable extinction is at work, with higher values to the northeast.

There exists a distinct radio continuum peak to the west of the radio arc named W49 South-1 (De Pree et al. 1997). There is no noticeable peak in the infrared emission from this source above that from the cometary UCH II emission in the SOFIA 20 μm data. It also seems not to be present in the Spitzer-IRAC data either, or at the infrared wavelengths observed by Smith et al. (2000). However, the extended emission near the peak of W49 South at 37 μm definitely protrudes out in this direction (Figure 3). While the peak of infrared emission in the IRAC and SOFIA bands seems colocated with the peak of the radio arc of the cometary UCH II region, the Herschel 70 μm peak

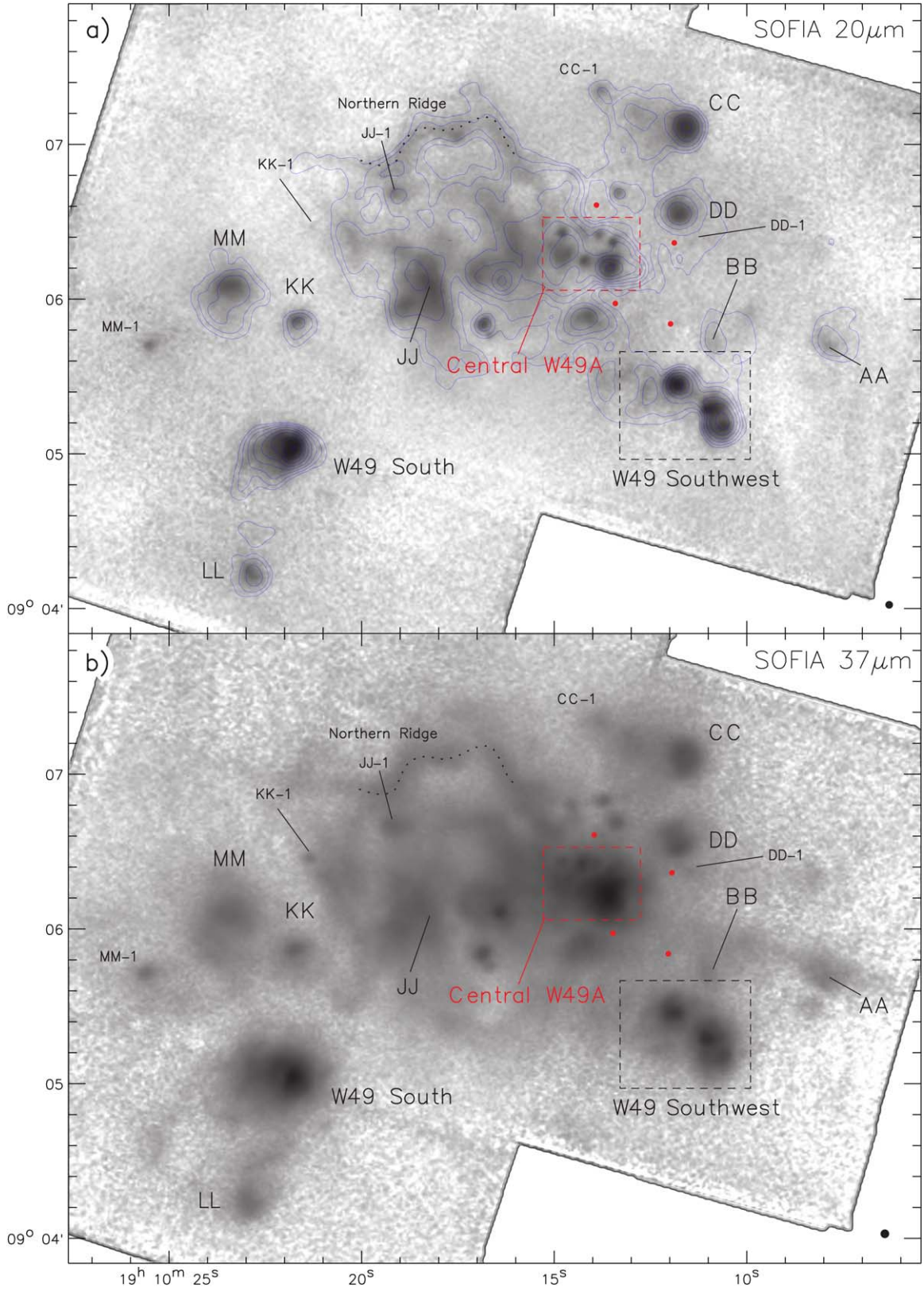

Figure 2. W49A image mosaic taken at (a) 20 μm and (b) 37 μm by SOFIA shown in inverse gray scale (i.e., brighter features are darker in color). The light-blue contours in the top panel are the 3.6 cm radio continuum emission from De Pree et al. (1997). All sources are labeled except in the higher source-density areas, where only the region name is given (dashed boxes). For the W49 Southwest region, see Figure 6, and for the Central W49A region, see Figure 10 for more details and to see the individual sources labeled within those areas. The curvy dotted line represents the location of the Northern Ridge. The red dots are the locations of the sources identified in Smith et al. (2000) as (going north to south) EE East, DD South, HH West, and BB East. The black dot in the lower right of each panel indicates the resolution of the image at each wavelength.

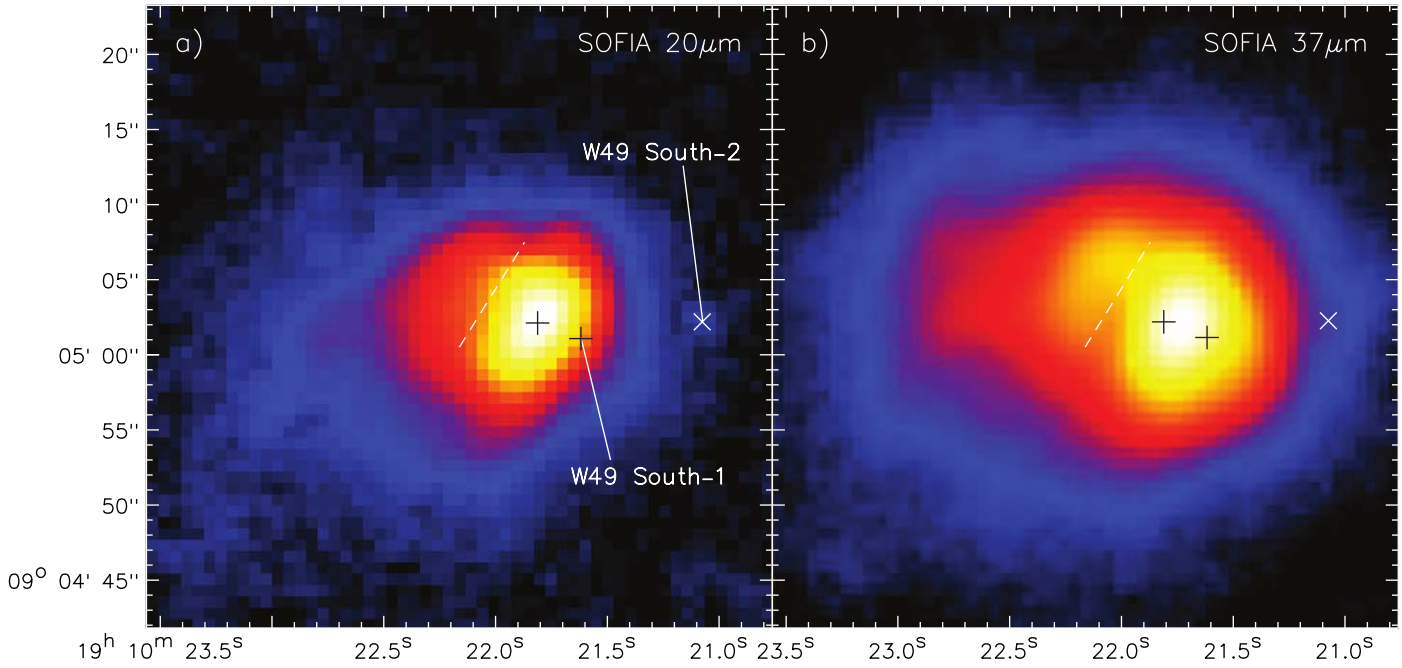

Figure 3. W49 South with false-color images showing emission at (a) SOFIA 20 μm and (b) SOFIA 37 μm. The black crosses show the locations of the cm radio continuum peaks for W49 South (east cross) and W49 South-1 (west cross). Newly identified infrared source W49 South-2 is marked with an $\times$. The location of the dark lane discussed in the text is indicated by the dashed white line.

seems to be offset toward W49 South-1 (Figure 4). This may signal that this source is highly embedded and becomes a more important contributor to the bolometric luminosity of the region at longer wavelengths. Given the implied higher levels of extinction to the north and west of the radio arc, it is likely that the large-scale morphology of W49 South is due to a champagne-like flow as suggested by Kim et al. (2018), rather than a bow shock from a moving source as was suggested by De Pree et al. (1997).

Homeier & Alves (2005) find 13 massive star candidates here in a revealed cluster they call Cluster No. 2 (Alves & Homeier 2003), likely from an earlier epoch of star formation. Saral et al. (2015) claim to find no YSOs or MYSOs in the W49 South region; however, given its large size ($d \sim 1.6$ pc) and our derived luminosity ($1.6 \times 10^4\,L_{\odot}$) W49 South must contain at least one MYSO. Saral et al. (2015) do identify several unclassified near-infrared sources in the area (Figure 4). Nine of these sources are located within or projected against the extended mid-infrared-emitting region of W49 South. The only one of these sources that is present and resolved from the extended emission in our SOFIA data is a source we call W49 South-2 (Figures 3 and 4), which can be seen clearly in the Spitzer-IRAC bands as well as our 20 μm image. At 37 μm there is an extension toward this region in the extended emission, but no clear source peak can be ascertained. Our SED modeling indicates that this source is also likely to be an MYSO, but because it is not emitting at cm radio continuum wavelengths it may be at an early evolutionary stage prior to the onset of a UCH II region.

3.1.2. W49 Southwest

The centimeter radio continuum regions R, S, and Q have been collectively referred to as W49 Southwest. The radio source R was further divided into three subcomponents or peaks by De Pree et al. (1997), named R, R_2, and R_3. All of these radio peaks are seen as peaks or extensions in the deconvolved infrared emission in the SOFIA 20 and 37 μm data (Figure 5). Images at all the infrared wavelengths seen by Spitzer-IRAC and SOFIA look fairly similar to the centimeter radio continuum emission (De Pree et al. 1997), with the peaks and extended emission aligning fairly well. One of the largest distinctions between the centimeter radio continuum images and SOFIA infrared images is that the bright and unresolved radio peak R is not the same location as the brightest infrared peak in the R region. There is an unresolved radio continuum source $\sim$3″ to the southwest of the R source (Figure 6(d)) that was not identified by De Pree et al. (1997) that we will refer to as R_4 (in keeping with the radio source nomenclature). This appears to be the radio peak that is associated with the brightest mid-infrared peak in the region. Additionally, we do see mid-infrared peaks in the deconvolved 20 and 37 μm data that correspond to the approximate locations of radio peaks R, R_2, and R_3 (see Figure 5). The R_4 source appears to dominate the region's emission at longer wavelengths, becoming brighter than source S at 37 μm, and appearing to be the closest source location to the bright peak seen at 70 μm (Figures 6(c) and (d)).

While there is no definitive peak at the location of R in the Spitzer-IRAC data, the deconvolved SOFIA 20 μm data show a definite peak at this location, and the deconvolved 37 μm data show a bright protrusion of emission in this direction (Figure 5). R_2 shows the opposite behavior, with a protrusion toward this location at 20 μm, and a definitive peak seen at this location at 37 μm. Source R_3 is never really seen as a peak in the near- to mid-infrared and looks to be extended emission unresolved from and protruding to the west of source R_4.

Source S is the brightest infrared source in this subregion of W49A at wavelengths less than 20 μm and looks similar at all infrared wavelengths, and similar to the centimeter radio continuum emission seen by De Pree et al. (1997). At all infrared wavelengths, its core is elongated E–W, with a peak offset to the western part of the elongation. There is an arm of

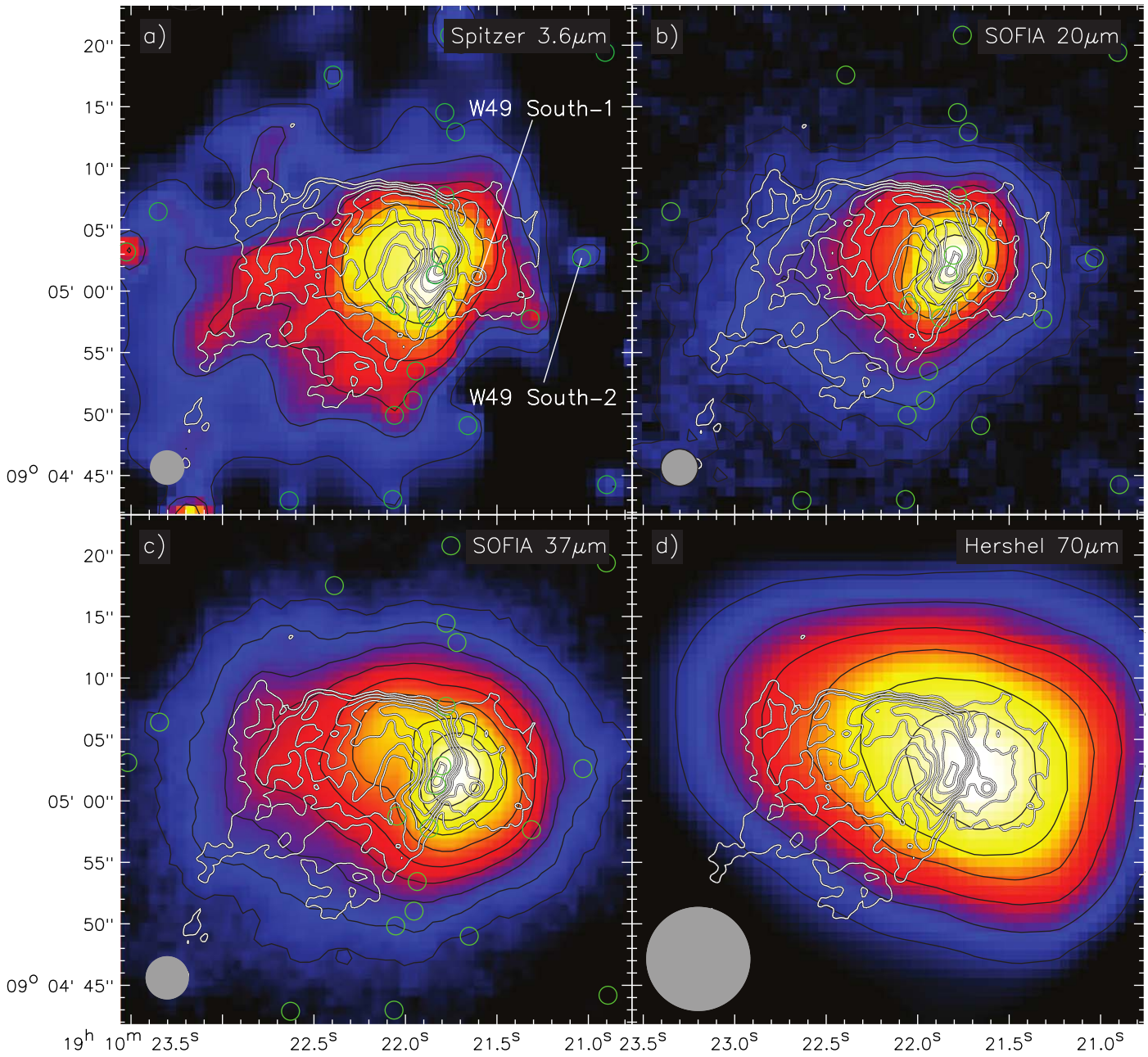

Figure 4. W49 South with false-color images and thin black contours showing emission at (a) Spitzer 3.6 μm, (b) SOFIA 20 μm, (c) SOFIA 37 μm, and (d) Herschel 70 μm. Overlaid on each panel are the 3.6 cm radio continuum contours from De Pree et al. (1997) as white contours, and the locations of near-infrared point sources identified by Saral et al. (2015) are indicated by the green circles. The resolution at each wavelength is shown by the gray circle in the lower-left corner of each panel.

extended emission coming off of the eastern edge of the elongated core pointing toward the northwest, which is best seen in the 37 μm deconvolved image (Figure 5(b)). In radio centimeter continuum emission there is also an arm to the northwest coming off of source S (see radio contours in Figure 5), but it does not seem to be colocated with the 37 μm emission arm; this may be due to variable extinction or external heating of the arm.

Source Q in the radio appears to be two parallel lobe-like structures elongated southeast to northwest with a lane of lesser emission in between (see De Pree et al. 1997, and Figure 5). At infrared wavelengths we see extended emission throughout the same area covered by the radio continuum emission, and though the parallel lobe structures in the radio continuum are not as pronounced in the infrared, we do see relatively less infrared emission in the same location as the lane of decreased emission seen in the radio. This is contrary to what was reported by Smith et al. (2000) who state that the peak emission at mid-infrared wavelengths is coincident with a relative minimum at the center of the radio emission of Q. This was because their mid-infrared images were aligned to the radio continuum images by aligning the peak of infrared emission in the R region with the radio peak of source R, and not R_4; therefore, their astrometry is offset from ours by about 3″. There is infrared emission within each of the parallel and elongated radio lobes, and while they do not peak in the same location as the radio lobes, they do seem to have the same position at all Spitzer-IRAC and SOFIA wavelengths

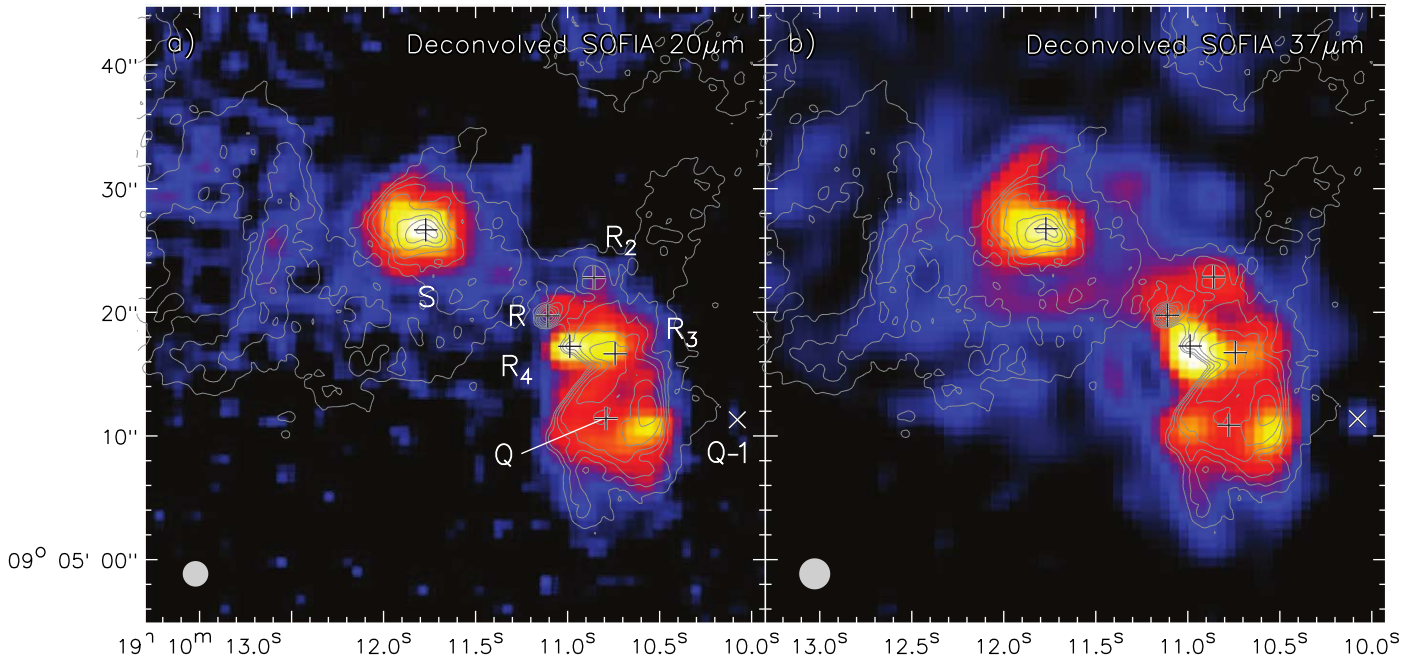

Figure 5. W49 Southwest with false-color images showing emission at (a) SOFIA 20 μm and (b) SOFIA 37 μm. The 3.6 cm radio continuum contours from De Pree et al. (1997) are overlaid on each panel with crosses showing the locations of the cm radio continuum peaks, with the names of the peaks indicated. The location of the newly identified infrared peak Q-1 is shown by the $\times$ symbol. The resolution at each wavelength is shown by the gray circle in the lower-left corner of each panel.

(Figure 6). Smith et al. (2000) state that the morphology of the infrared emission from source Q looks like an edge-on torus at certain wavelengths, but it is unclear from our data if that is the case or not. Situated approximately 10″ to the west of the center of Q is a source resolved from the rest of the extended emission of the Q region at both SOFIA wavelengths, but it is best seen at 37 μm, which we call Q-1 (Figure 5(b)). It is also faintly visible in the IRAC images and was listed as a potential YSO candidate by Saral et al. (2015). Our SED fits to the photometry of Q-1 indicate that it is likely to be an MYSO ($M = 8$–$12\,M_{\odot}$), though there is no radio continuum emission coming from the source. It may be an MYSO at a stage prior to the onset of a UCH II region.

The whole region surrounding W49 Southwest is pervaded by multiple near-infrared sources (Homeier & Alves 2005; Saral et al. 2015, and see Figure 6), which Homeier & Alves (2005) suggest are from a previously formed cluster of stars associated with the UCH II regions of S, R and Q. Because the near-infrared sources have no significant mid-infrared emission (indicating no appreciable circumstellar dust) as seen in the SOFIA data, they are likely not massive YSOs and might not even be YSOs (i.e., they could be main-sequence stars). This would add credence to the suggestion by Homeier & Alves (2005) that the stars forming in the UCH II regions now are likely not the first generation to form in the area.

3.1.3. W49A/CC/DD/DD South

At centimeter radio continuum wavelengths, the brightest area of emission of CC has a core-halo morphology, with a more prominent arc on the western side, and a core with a peak offset to the east (De Pree et al. 1997). The core of CC is claimed to be an MYSO candidate by Saral et al. (2015). This bright core-halo structure is at the apex of a fan-shaped region of faint and diffuse emission that extends ~40″ to the east and widens with distance from the CC peak. The bright core-halo structure is mimicked to some degree at all of the infrared wavelengths, though at 37 μm the peak is very broad and the halo is not well resolved, even in the deconvolved data. Extended low-level infrared emission is seen throughout the fan-shaped extended emission of the CC region, but the knots change position with infrared wavelength and do not match up with the radio knots very well, indicating that these structures are likely to be externally heated and ionized knots of dust and gas. However, one peak within this extended region of emission, located ~35″ east of the peak of CC and which we label as CC-1 in Figure 7, appears to be present in all Spitzer-IRAC bands as well as the SOFIA wavelengths. Our SED modeling shows that it is likely to be a MYSO.

For source DD, the 37 μm emission of looks more similar to its radio continuum emission morphology than to its 20 μm image. DD has a bipolar appearance in the centimeter radio continuum images of De Pree et al. (1997), though both lobes appear flattened and the southern lobe is considerably brighter than the northern lobe (Figure 8). In the SOFIA images, the northern lobe is more prominent at 37 μm than at 20 μm; however, like the radio continuum emission, the southern lobe is brighter than the northern lobe at both infrared wavelengths. In the Spitzer-IRAC data, the southern lobe is also the most obvious. Given its large size ($d \sim 0.7$ pc), source DD is too large to be considered even a CH II region ($\sim 0.1 < d < 0.5$ pc; Mezger et al. 1967). However, given the complex substructure, the large calculated luminosity of the source from our data ($\sim 2.0 \times 10^5\,L_{\odot}$) and the bright centimeter radio continuum emission, this H II region must house at least one MYSO.

Mid-infrared observations of the DD area by Smith et al. (2000) reveal another bright and extended source of emission about 10″ south of DD, which they call DD South. They claim clear detections of this source at all four mid-infrared wavelengths they observed (12.3, 12.8, 13.2, and 20.6 μm), with the integrated flux from the source at 20 μm (~80 Jy) being twice as bright as their measured 20 μm flux from source

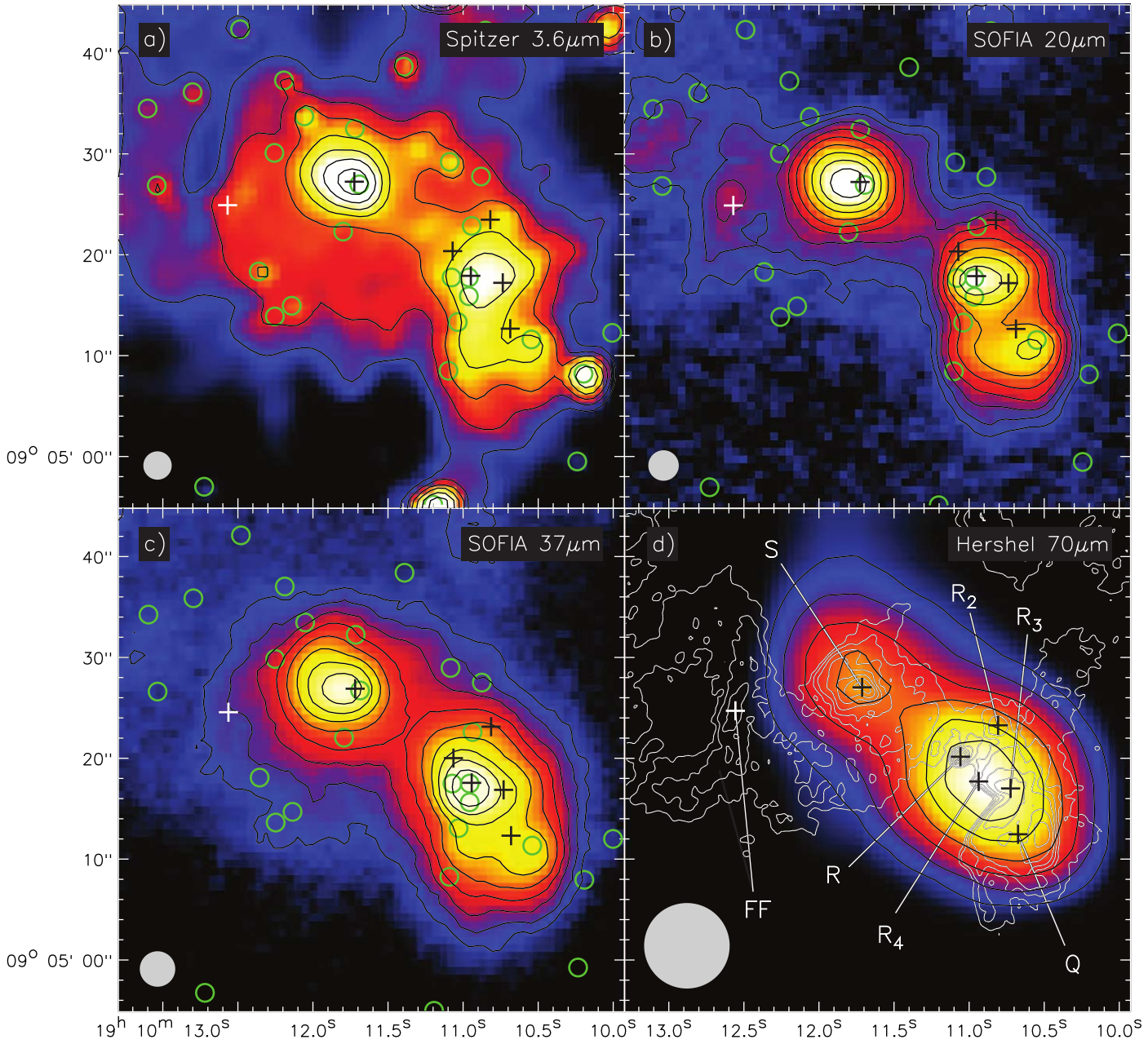

Figure 6. W49 Southwest with false-color images and thin black contours showing emission at (a) Spitzer 3.6 μm, (b) SOFIA 20 μm, (c) SOFIA 37 μm, and (d) Herschel 70 μm. The crosses are the peaks of the 3.6 cm radio continuum sources from De Pree et al. (1997), and the locations of near-infrared point sources identified by Saral et al. (2015) are indicated by the green circles. The 3.6 cm radio continuum contours are shown along with the labels for the centimeter radio sources in panel (d). The resolution at each wavelength is shown by the gray circle in the lower-left corner of each panel.

G. They observe DD South as an irregular or core-halo morphology (similar to source S) with a diameter of about 12″. We do not detect this source at either SOFIA wavelength (see red dots in Figure 2), and it is not present in the Spitzer-IRAC images. Given the large brightness claimed by Smith et al. (2000) for DD South at 20 μm, our lack of a detection in the SOFIA 20 μm image is not due to our observations having a shallower detection limit. Because it has never been seen before in the infrared, DD South could be a flaring source, as has been seen in MYSOs like NGC 6334I (Hunter et al. 2018). However, as we discuss in a later Section 3.1.6, it seems more plausible that this is an artifact in the data or produced in the data reduction and not a real source, because we also fail to detect the three other new infrared sources identified by Smith et al. (2000).

3.1.4. Central W49A: Welch Ring Sources

The central region of W49A contains more than two dozen identified centimeter radio continuum sources within 1 arcm^2. The most prominent sources are grouped into a feature known as the Welch Ring (Welch et al. 1987), and most of these sources are thought to be individual UCH II regions (however , as we will discuss later in this section and more in Section 4.1, several of them may not be).

Smith et al. (2000) pointed out that while many of these radio sources are detectable in the infrared, not all of them are. They posit that it is very likely that the extinction toward the western side of the ring of sources has such a high level of obscuration that the material is too optically thick even for their mid-infrared photons to be seen. They point to observations

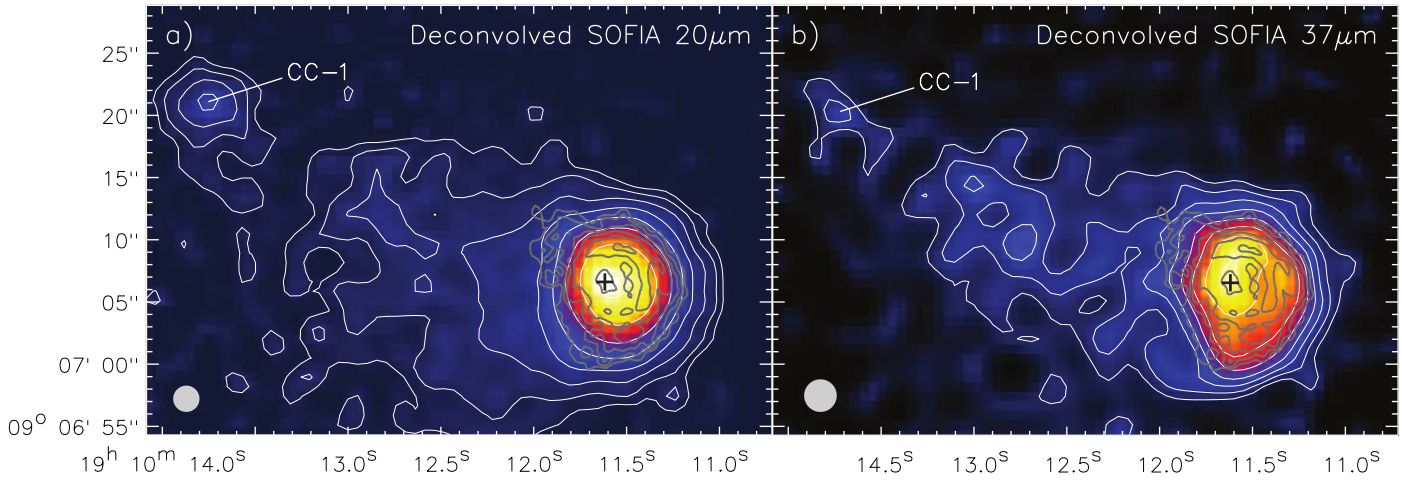

Figure 7. W49A/CC with false-color images and thin white contours showing deconvolved emission at (a) SOFIA 20 μm and (b) SOFIA 37 μm. Overlaid in gray on each panel are the 3.6 centimeter radio continuum contours from De Pree et al. (1997); however, only the brightest five contours are shown to isolate the bright core-halo radio structure. The black crosses show the radio peak position. The resolution at each wavelength is shown by the gray circle in the lower-left corner of each panel.

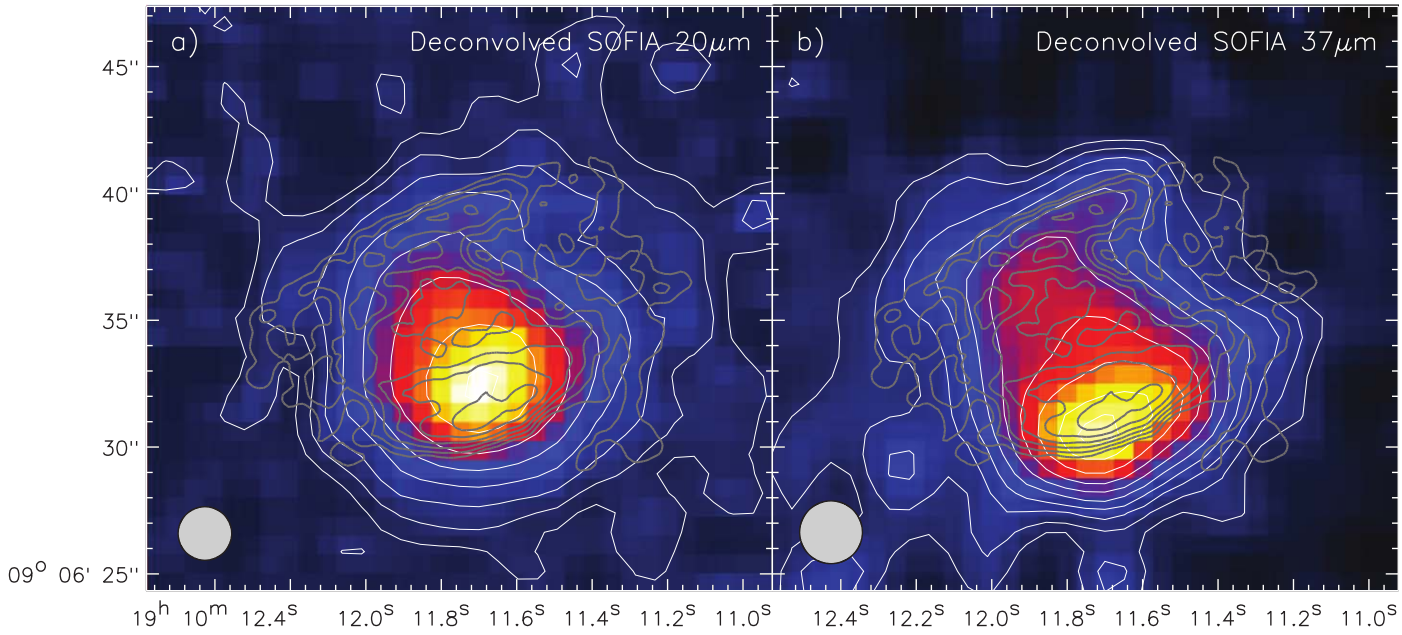

Figure 8. W49A/DD with false-color images and thin white contours showing deconvolved emission at (a) SOFIA 20 μm and (b) SOFIA 37 μm. Overlaid on each panel are the 3.6 cm radio continuum contours from De Pree et al. (1997) as gray contours. The resolution at each wavelength is shown by the gray circle in the lower-left corner of each panel.

toward this region using molecular lines that show a higher concentration of molecular material on the western side of the ring (e.g., Serabyn et al. 1993; Jackson & Kraemer 1994). Like Smith et al. (2000, 2009) we do not detect infrared emission coming from radio sources A or B at 20 or 37 μm (Figure 9), nor are they seen in any of the Spitzer-IRAC bands. There is a weak infrared peak located 2″ to the west of A in all of the Spitzer-IRAC bands; there is also emission here at 37 μm. In fact, at 37 μm we detect extended emission around sources A and B, with deficits in emission exactly at their locations. This likely means that, in addition to the high levels of environmental extinction (i.e., from the large-scale molecular cloud structure), the self-extinction from circumstellar dust (i.e., disk and/or envelope material) for these sources may be a significant component in the overall level of extinction. This is most evident for source B, where there is a ring of mid-infrared emission at 37 μm all around the source, but a dip in the emission right where the radio source peak is located (see Figure 9(d)).

Smith et al. (2000, 2009) do not detect emission from radio sources B_1, D, or E. We also do not detect any point-like emission from the locations of these sources in our deconvolved 20 μm image. In the deconvolved 37 μm image there is extended emission toward these locations, and while it is possible that this is unresolved emission from the very bright G source, contributions to the emission in these areas due to sources B_1, D, and/or E cannot be ruled out. Interestingly, sources C and C_1, which also were not detected by Smith et al. (2000, 2009) at shorter mid-infrared wavelengths, appear to be associated with a protrusion of emission seen only at 37 μm,

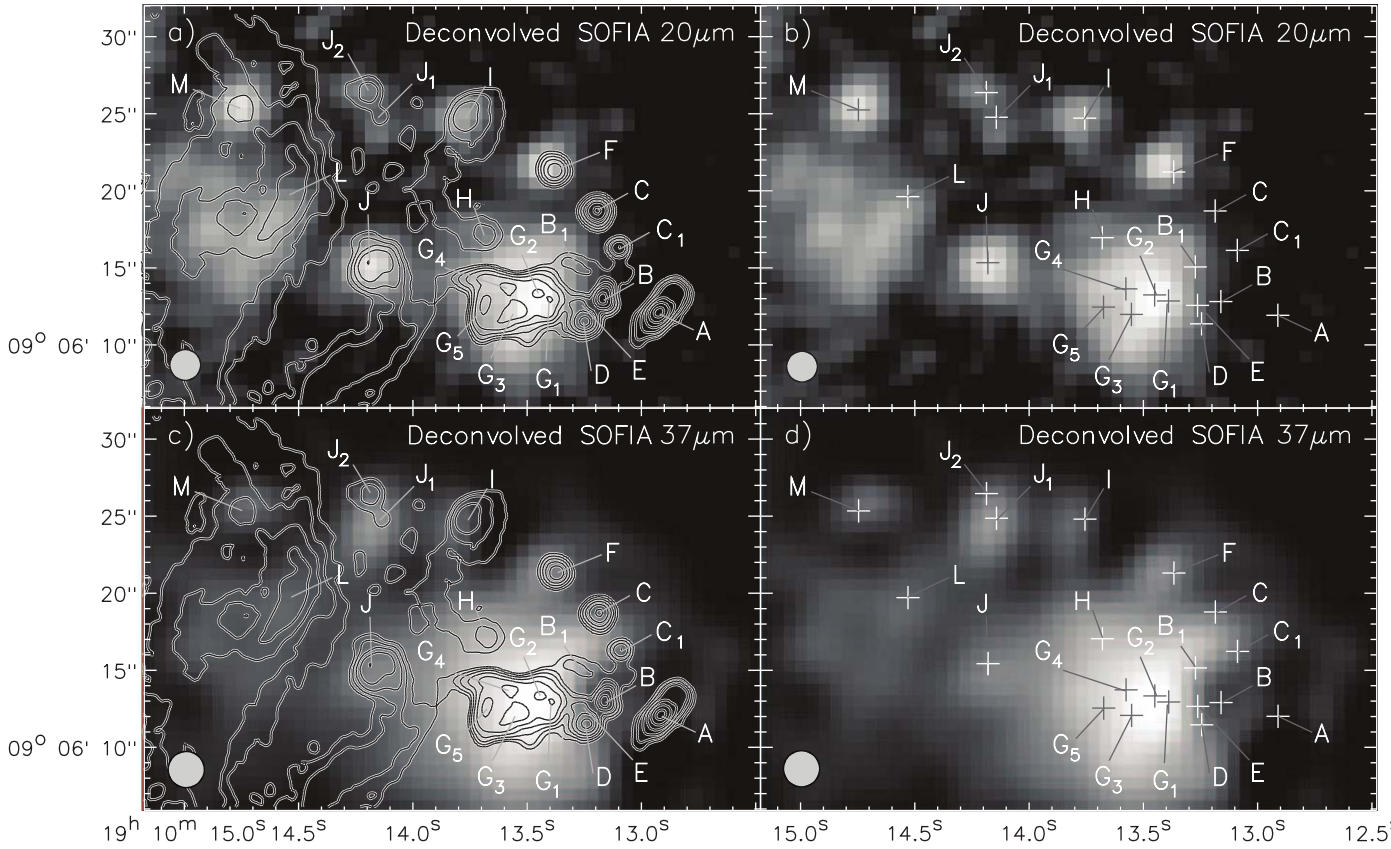

Figure 9. Gray-scale images of the "Welch Ring" area of W49A with deconvolved emission as seen by SOFIA at 20 μm (top row) and 37 μm (bottom row). The left-column panels have overlays of the 3.6 cm radio continuum emission from De Pree et al. (1997) as gray contours with their peaks labeled. In the right column of panels, the radio peak locations are indicated by the crosses. The resolution at each wavelength is shown by the gray circle in the lower-left corner of each panel.

though the brightest emission is located between the two sources, with the radio source peaks lying on the periphery of the infrared emission (see Figure 9(d)). It could be that this infrared emission is not tracing emission coming from the exact locations of C or C_1 due to elevated levels of extinction directly along the line of sight to their radio peaks, but instead leaking out of an area of lesser extinction between them.

Source F is the brightest source in the area in the Spitzer-IRAC images at 3.6 and 4.5 μm, but G becomes more prominent at longer wavelengths, though F is still detected in our SOFIA data at both 20 and 37 μm. Our SED modeling of this source results in a rather low luminosity and not an MYSO. As we discuss in detail in Section 4.1, the radio emission from source F is likely not due to free–free emission from a UCH II region, but instead from nonthermal synchrotron emission (likely from an outflow).

Radio source G was resolved into five individual peaks by De Pree et al. (1997) named G_1 to G_5 (Figure 9). The higher spatial resolution follow-up observations at 3.6 cm by De Pree et al. (2020) show that sources G_1 and G_2 break up even further into compact radio continuum objects (with source "G2a" being the brightest) and that G_3, G_4, and G_5 are not likely individual YSOs, but arcs of radio continuum emission tracing the edges of a more coherent cavity structure with a diameter of about 3″. Like Smith et al. (2009) saw at 18.5 μm and Smith et al. (2000) saw at 20.6 μm, we do not resolve any of these subcomponents at 20 and 37 μm with SOFIA, and source G looks like a cometary H II region whose peak is at the location of the G_2 radio peak. G_2 is also a compact infrared source in all Spitzer-IRAC bands. We cannot resolve out mid-infrared sources associated with any other radio peak, even in the deconvolved data, and the region of brightest mid-infrared emission covers an area that encompasses all five radio peaks. However, the overall morphology of the extended infrared emission looks different than what is seen in the radio. The east–west extent is comparable in the two wavelength regimes; however, the centimeter radio continuum emission drops off precipitously both to the north and south, whereas in the mid-infrared (especially evident at 37 μm) there is extended emission to the north and south (see Figures 9 and 10).

Source H can be seen as a broad, weak peak of emission in the Spitzer-IRAC bands at 3.6 and 4.5 μm. At the other two IRAC wavelengths, saturation effects from sources F and G overwhelm the region. In the 20 and 37 μm SOFIA images, H appears as a protrusion of unresolved extended emission from G (Figure 9). Radio sources I and J are seen at all infrared wavelengths from Spitzer 3.6 μm out to 37 μm. At 37 μm, source J is partially resolved from the extended emission of source G (Figure 9).

Radio sources J_1 and J_2 are only $\sim$2″ apart, with J_2 being the brighter of the two sources. In the Spitzer-IRAC images, there is an infrared source that is elongated north–south with the northern half colocal with the peak of J_2. However, J_1 lies about 1.″5 southwest of J_2, so this southern half of the north–south elongated infrared emission seen with IRAC does not seem to be colocal with J_1. In the SOFIA deconvolved 20 μm image, there are two separated sources, with the northern source at the location of J_2, and the other not quite at the location of J_1 (Figure 9). At 37 μm there does not appear to be emission coming from J_2, but the peak is on the southern half

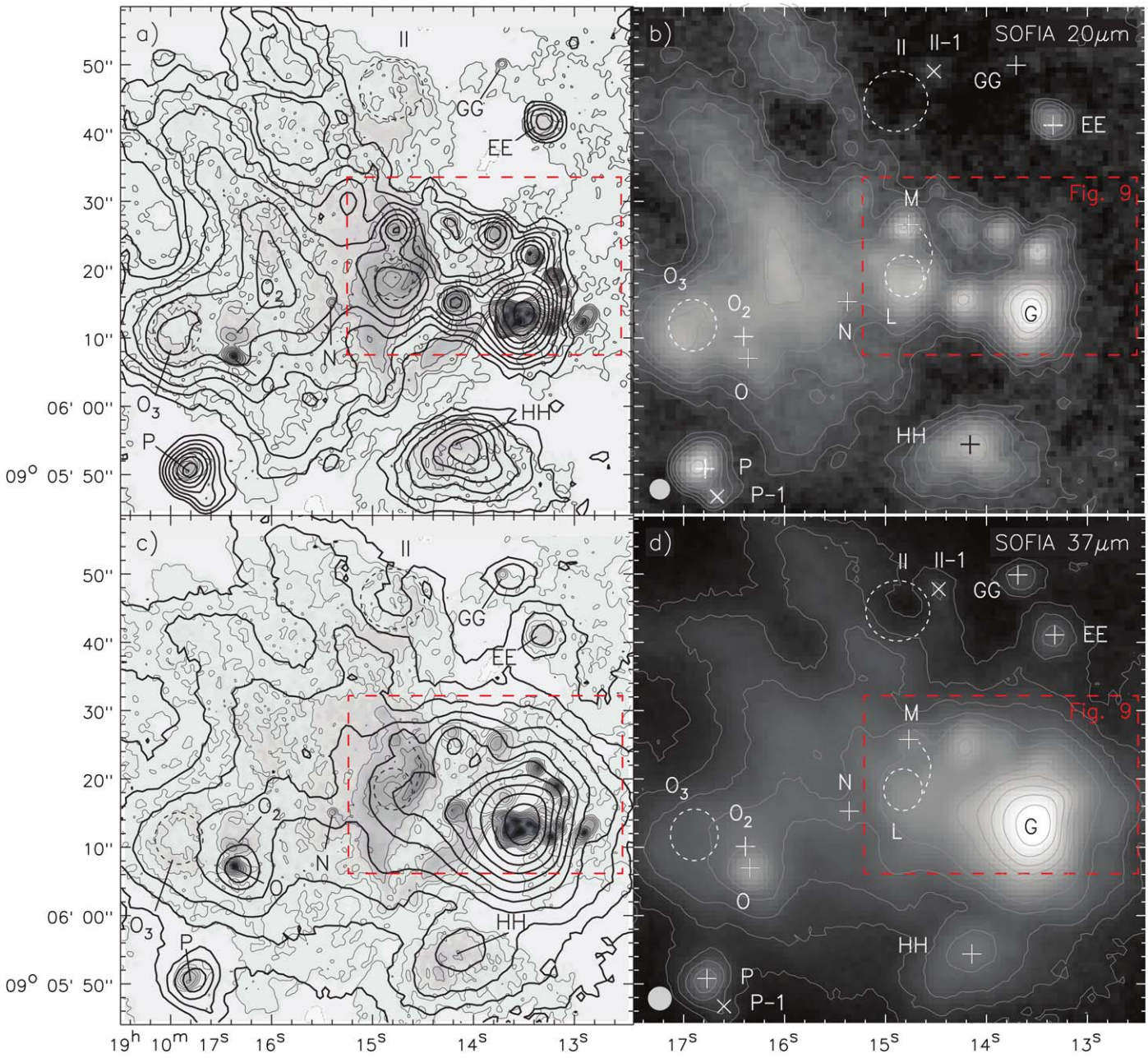

Figure 10. Images showing the central region of W49A. (a) The inverse gray-scale image with light gray contours shows the 3.6 cm radio continuum emission from De Pree et al. (1997) overlaid with the 20 μm emission from SOFIA as thick black contours. (b) A gray-scale image with light gray contours shows the 20 μm emission seen with SOFIA. (c) Same as (a) except the overlaid thick black contours are the 37 μm emission from SOFIA. (d) A gray-scale image with light gray contours shows the 37 μm emission seen with SOFIA. The location and sizes or the radio sources with ring-like appearances are shown by the dashed circles, and the location of the newly unidentified infrared sources are given by the $\times$ symbols. The sources within the red dashed box in all panels are not labeled, but this area is discussed in detail in Figure 9.

of the elongated near-infrared source seen with Spitzer-IRAC. This points to the possibility that J_1 is the more embedded or least evolved of the two sources.

In the radio, source L appears as a bright arc of emission that terminates to the south as the western side of a ring-like structure of emission, giving the overall appearance of a letter "d" (Figure 9). The north half of the radio arc is not traced by infrared emission; however, the ring-like structure is relatively bright at all wavelengths from 3.6 to 37 μm. However, as the locations of the clumps that make up the ring structure do change with infrared wavelength, these structures are likely to be externally heated knots, rather than individual YSOs.

Radio source M is seen at all Spitzer-IRAC and SOFIA wavelengths and appears as a prominent compact point-like infrared source (Figure 9).

3.1.5. Central W49A: Other sources

Compact radio sources EE and GG lie to the north of the Welch Ring (Figure 10), and while EE is detected as a compact infrared source at all wavelengths from 3.6 to 37 μm, the GG radio source is prominent only as a compact point source at 37 μm and is not detected at 20 μm or shorter wavelengths. In the Herschel 70 μm image, source GG can be seen as a nearly resolved source north of the extended emission from the Welch

Ring. This is consistent with GG being a very young, self-embedded MYSO. Our SED modeling does seem to confirm its massive nature (best fits yielding $M = 16$–$24\,M_{\odot}$).

Radio source II also lies just to the north of the Welch Ring (Figure 10) and is seen as a weak partial ring of emission at centimeter radio wavelengths. This source only seems to have some weak emission in our 37 μm image, even weaker emission at 20 μm, and is not seen at shorter wavelengths. There does seem to be a point-like infrared source in the northwestern part of the ring, about 12″ east of GG, which we label II-1. This source is seen at all IRAC wavelengths, and our SED model fits show it to be an MYSO candidate. Given that this source has no detected centimeter radio continuum peak at this location would imply that II-1 is a very young MYSO in a phase prior to the onset of a UCH II region. Our SED model fits imply it has a stellar mass of $M = 8\,M_{\odot}$.

The compact radio sources N and O also appear to be highly embedded sources lying to the east of source G (Figure 10). In the Spitzer-IRAC data and the SOFIA data, N is only seen at 37 μm. In the Herschel image at 70 μm, there is a protrusion of emission from the extended G source toward this location and is thus likely associated with it. For source O, the shortest wavelength it is detected is at 5.8 μm, though it is a relatively weak source at wavelengths 20 μm and shorter. It becomes one of the brightest sources in the central W49A area at 37 μm and is easily visible in the Herschel 70 μm image. Again, a lack of short-wavelength emission and very bright far-infrared emission would indicate that these are both very young, self-embedded MYSOs (which our SED model fitting seems to confirm).

Also to the east of G are radio sources O_2 and O_3 (Figure 10). The radio peak of O_2 is just north of O (∼3″ away), surrounded by a fan-shaped region of extended radio continuum emission. There is no peak seen at the radio peak of O_2 at any infrared wavelength, and while there is some emission at each wavelength in the region, it looks different at each wavelength, signifying that we are likely seeing infrared emission from the diffuse dust in the overall cloud, and not emission coming directly from a YSO. Radio source O_3 is a ring of emission about 4″ in radius, and we see a similar ring structure at both 20 and 37 μm.

P is a bright source elongated at a position angle of 135° in the SOFIA images, with a second, much fainter infrared source located ∼5″ away to the southwest, which we label P-1 (Figure 10). Source P is associated with a compact radio continuum source, while P-1 is associated with a weak knot of radio continuum emission in the 3.6 cm data. Both sources can be seen from 3.6 μm out to 37 μm, and there is even emission seen here at 70 μm, though it is hard to tell, given the resolution of the Herschel data, if emission is coming from both sources or not. We find from our SED model fitting that P is an MYSO and P-1 is an intermediate to high-mass YSO.

To the south of the G region lies radio source HH (Figure 10). It is a large (∼15″ × 10″) triangular-shaped feature whose broad peak is the same from 3.6 to 37 μm. HH might be a region containing multiple unresolved MYSOs given its large size and the relatively high luminosity we derive for it from our SED model fitting (i.e., $\sim 2.6 \times 10^5\,L_{\odot}$).

3.1.6. Other Sources in W49A

Radio sources AA and BB are large ($d \sim 20''$), weak, and extremely diffuse radio continuum regions (De Pree et al. 1997) with a faint ring or bubble-like appearance at 3.6 cm. The infrared emission extends over a comparable region to the radio at all infrared wavelengths from 3 to 37 μm. In the SOFIA images, AA and BB appear as only faint patches of diffuse emission with highly broadened peaks at both 20 and 37 μm within which we can see no clear substructure (Figure 2). We derived luminosities for AA and BB in the same manner as we did for other extended sources (i.e., in Section 4.2.1) and find that AA has a luminosity of only $\sim 6 \times 10^4\,L_{\odot}$ (the equivalent of a B0 star) and BB has a luminosity of only $\sim 1 \times 10^5\,L_{\odot}$ (the equivalent of a O9 star). Given their large, bubble-like radio morphologies, their relatively low infrared-derived luminosities, and their lack of compact and/or bright infrared or radio components or peaks, AA and BB may be more evolved H II regions. Indeed, AA and BB have by far the lowest emission measures (EM) in W49A ($\mathrm{EM} \sim 7$–9×10^5 cm^{-6} pc; De Pree et al. 1997) and combined with their large sizes ($d > 1.0$ pc), they do not have properties consistent with cH II regions ($\sim 0.1 < d < 0.5$ pc; $\mathrm{EM} > 10^8$ cm^{-6} pc; Mezger et al. 1967) and are more in line with the properties of evolved H II regions (e.g., Sh2-90; Samal et al. 2014). Consistent with this hypothesis, inspection of our multiwavelength data of AA and BB reveals that both have an unresolved near-infrared source centrally located within their extended radio continuum regions. We cannot be completely certain if these sources are foreground stars, independent YSOs, or actually the central ionizing sources of the AA and BB H II regions; however, from the limited data available, they do appear to have characteristics consistent with being the central ionizing stars. For AA, the stellar source peak is located at $\alpha_{\mathrm{J2000}} = 19{:}10{:}07.7$, $\delta_{\mathrm{J2000}} = +9{:}05{:}45$, and for BB, the source peaks at $\alpha_{\mathrm{J2000}} = 19{:}10{:}10.6$, $\delta_{\mathrm{J2000}} = +9{:}05{:}45$ and both are only detected in the Spitzer 3.6 and 4.5 μm data. Neither source is detected at shorter wavelengths (i.e., in optical POSS2 images and 2MASS $J/H/K$ images), which would be expected of stars at the distance of W49A due to the high line-of-sight extinction and not of nearby foreground stars. Neither source is detected at Spitzer 5.8 or 8.0 μm nor in our SOFIA data, signifying sources with no circumstellar emission (i.e., consistent with revealed stars and not YSOs).

Another newly identified infrared source we name DD-1 is located ∼13″ southwest of the peak of DD (Figure 2), with a faint peak surrounded by some modest extended infrared emission. This source is seen in all IRAC bands as well as with SOFIA. The SOFIA 20 μm image shows a point source, whereas the 37 μm image shows more of an extended source, but in both cases the source is faint. Again, the Herschel 70 μm image shows a tongue of emission toward this area, as does the image at 3.6 cm given in De Pree et al. (1997), although with very faint surface brightness. Our SED modeling reveals this source to be an MYSO.

Radio source FF is a very faint partial ring of emission ($r \sim 7''$) whose western side is the most prominent arc, with a fainter arc on the eastern side (Figure 6). Similarly, this is the case in the infrared, and the ring is better seen at 20 μm than 37 μm. It could be that is because this side of the ring is close to the very bright source S, which may be responsible, at least in part, for heating it (Figure 6). Indeed, the western side of FF can be seen even down to 2 μm (Alves & Homeier 2003).

The large and bright radio source JJ at low resolution approximates a 20″ × 30″ rectangular shape (Figure 2). The shape and size are grossly mimicked in the infrared, though the

northeastern corner of the radio continuum region is depressed in infrared emission and the brightness distribution within the entire radio-emitting area fluctuates markedly with infrared wavelength. There are no well-defined peaks present that are colocal at near-infrared and mid-infrared wavelengths, though the radio peaks toward the northern corner of the triangle, perhaps indicating the location of the MYSO(s) that are heating the entire clump.

The north-central region of W49A has a long (>1′) ridge of emission snaking along at about the same decl. east to west (Figure 2). This ridge is easy to spot at all IRAC and SOFIA wavelengths, and even at wavelengths as long as 70 μm (with Herschel) and as short as 2 μm (Alves & Homeier 2003). There is also radio continuum emission coming from this ridge at centimeter wavelengths, and we labeled this the "Northern Ridge" in Figure 2. This could be a radiation-driven ridge of material snowplowed by the combined emission of the O stars south of it. This would be consistent with the picture of W49A by Peng et al. (2010), where two expanding shells are responsible for some of the large-scale morphology of the region.

Just south of the Northern Ridge on the eastern side is an infrared source we newly identify here as JJ-1 (Figure 2). It is the only semicompact infrared source that we can identify as a potential star-forming clump in or near the Northern Ridge. It is seen at all infrared wavelengths from IRAC to 70 μm Herschel data. Though it is hard to see in Figure 2, at 37 μm the source appears as an arc shape with a broad peak offset to the southeast. At 20 μm the source appears more point like and peaking toward the center of the infrared-emitting region. Interestingly, in the IRAC bands the source is seen as two structures, an arc of emission (coincident with the 37 μm emission) and a point source (coincident with the 20 μm peak). The arc of emission could be a partial dust shell around the point source. The source does display 3.6 cm radio continuum emission comparable to the shape and extent of the 37 μm emission, indicating it harbors at least one MYSO.

To the east of JJ-1 lies an infrared source we label as KK-1 (Figure 2). It is an unresolved point source at all infrared wavelengths from IRAC 3.6 μm to SOFIA 37 μm, and there is even a tongue of emission in the extended Herschel 70 μm image toward this source. Though it displays no radio continuum emission, our SED modeling shows it to have the luminosity of an MYSO. Therefore, it may be an MYSO in a stage prior to the onset of a UCH II region.

Radio region KK has a radio peak coincident with peaks seen at all Spitzer-IRAC and SOFIA infrared wavelengths, as well as at Herschel 70 μm. KK is semicompact and our SED models show it to be an MYSO.

LL appears in the radio as a broad source with an ill-defined peak shaped like a kidney bean. This shape is mimicked in the infrared data. LL is situated at the end of a tail of infrared emission spurring off of W49 South toward the south (Figure 2). This tail is seen at all infrared wavelengths (though it is very faint in our 20 μm image), but only at 70 μm is the emission in the arm brighter than the emission of LL, peaking halfway between W49 South and LL.

The radio region MM is a large ($d \sim 25''$) radio continuum region at low resolution (De Pree et al. 1997) with a diffuse extension toward the southeast (Figure 2). This extension is also seen in the SOFIA 37 μm image of this source, whereas the morphology changes considerably at shorter wavelengths. The main peak in the SOFIA data looks like a horizontal bar or unresolved binary peak. The Spitzer 8 μm image shows a barely resolved double source here, and at shorter IRAC wavelengths there is a third peak located just to the south ($\sim 4''$) of the doublet, which dominates the shortest IRAC wavelengths.

Due to a larger field of view than that studied in De Pree et al. (1997) and Smith et al. (2000), we found a smaller ($d \sim 4''$) but resolved infrared source at both SOFIA wavelengths located about 58″ west of KK, which we label as MM-1 in Figure 2. The source appears point-like at 37 μm, but at shorter wavelengths there is diffuse but extended emission on both sides of the infrared peak at a p.a. of $\sim 135°$. At the shortest IRAC wavelengths, it appears almost rectangular or bow-tie shaped. This source is also seen as an unresolved source in the Herschel 70 μm image. Because MM-1 is also off the field of the archival 3.6 cm VLA data as well, it is unknown if this source is a centimeter radio continuum emitter. Given the large derived luminosity from our SED modeling, we conclude that this source is powered by at least one MYSO and the extended emission could be due to outflow cavities that are often seen in the mid-infrared (e.g., De Buizer 2006; De Buizer et al. 2017).

Smith et al. (2000) found four new mid-infrared sources named for their proximity to known sources: BB East, DD South, EE East, and HH West (see red dots in Figure 2). DD South is large ($d \sim 10''$) and estimated to be 80 Jy at 20 μm, and thus should be very obvious in or SOFIA images, yet it does not appear in either our 20 or 37 μm data nor is there a source there in any of the IRAC bands. Source BB East is about the same extent with a peak surface brightness of ~ 1 Jy arcsec^{-2}, which should also be easily detectable in our images, and yet nothing is present in either our 20 or 37 μm data or in any of the IRAC bands. EE east and HH west are much smaller and fainter sources; however, both are estimated to have a peak surface brightness of 0.25 Jy arcsec^{-2} at 20 μm, and so we should even be able to detect that level of emission with an S/N of ~ 30 in our 20 μm SOFIA data. However, we see no hint of either source in either SOFIA band, nor are there IRAC sources at these locations. Given that all of these sources should be easily detected in our images and are not, and given that none of the four sources have components in any of the IRAC bands either, it could be that none of these sources are real.

4. Results and Data Analysis

Tabulating the detections and nondetections from sources discussed in Section 3, we have produced Tables 1 and 2. Table 1 is a list of all previously known radio continuum sources, as given by De Pree et al. (1997). In this table, we identify in R.A. and decl. the aperture centers (not the source peaks or centers) used for the photometry of each source as well and the aperture radii used at each wavelength ($R_{\rm int}$). We give the integrated flux densities at both wavelengths within those apertures ($F_{\rm int}$), as well as background-subtracted estimates of the flux densities of sources. We apply the same aperture photometry practices as we did in our previous studies to ascertain the aperture sizes to use for flux extraction. To quickly summarize, we choose an aperture radius where the flux from the azimuthally averaged radial profile of a source just begins to level out. If the source is surrounded by extended emission, this background is only a local minimum. The background flux estimate is taken from the statistics of the data

Table 1
Observational Parameters of All Known Radio Continuum Sources in W49A

Source	R.A. J2000	Decl. J2000	20 μm				37 μm			
			FWHM ($''$)	R_{int} ($''$)	F_{int} (Jy)	$F_{int\text{-}bg}$ (Jy)	FWHM ($''$)	R_{int} ($''$)	F_{int} (Jy)	$F_{int\text{-}bg}$ (Jy)
A	19 10 12.88	9 06 12.0	ND	3.1	<0.06	⋯	ND	3.1	<71.3	<11.0
AA	19 10 07.77	9 05 44.2	diffuse	10.7	16.2	8.01	diffuse	10.7	58.8	42.0
B	19 10 13.14	9 06 13.0	U	1.5	<1.08	<0.73	U	1.5	<76.9	<74.9
B_1	19 10 13.26	9 06 14.9	U	1.5	<1.97	<0.90	U	1.5	<357	<355
BB	19 10 10.80	9 05 43.9	diffuse	7.7	9.32	3.09	diffuse	6.9	44.0	9.22
C	19 10 13.17	9 06 18.6	U	1.5	<0.93	<0.59	U	1.5	<172	<170
C_1	19 10 13.08	9 06 16.2	U	1.5	<0.79	<0.45	U	1.5	<152	<150
CC	19 10 11.53	9 07 05.8	diffuse	11.5	88.5	68.5	diffuse	11.5	284	241
D	19 10 13.24	9 06 11.2	U	1.5	<2.08	<1.74	U	1.5	<347	<345
DD	19 10 11.68	9 06 32.4	diffuse	10.7	47.0	27.3	diffuse	10.7	240	217
E	19 10 13.26	9 06 12.4	U	1.5	<2.26	<1.92	U	1.5	<372	<370
EE	19 10 13.25	9 06 41.0	4.48	5.4	6.46	2.45	5.97	4.6	40.9	27.4
F	19 10 13.39	9 06 21.6	4.09	3.1	5.81	2.45	PR	3.1	<144	<139
FF	19 10 13.19	9 05 25.6	7″ ring	13.8	45.4	14.2	7″ ring	13.8	<176	<143
G_{tot}[a]	19 10 13.50	9 06 11.6	8.51	7.7	45.9	33.5	9.21	9.2	3700	3410
GG	19 10 13.62	9 06 49.6	ND	3.8	<1.98	<0.18	4.45	3.8	22.8	11.1
H	19 10 13.69	9 06 17.1	U	1.5	<1.75	<1.43	U	1.5	<321	<319
HH	19 10 14.07	9 05 51.7	diffuse	10.7	39.9	16.9	diffuse	9.2	251	91.2
I	19 10 13.76	9 06 24.4	4.46	3.1	4.18	1.49	4.6	2.3	53.2	38.1
II	19 10 14.96	9 06 43.1	4″ ring	12.3	26.7	9.29	4″ ring	12.3	268	136
J	19 10 14.18	9 06 14.6	4.56	3.8	9.29	4.20	PR	3.8	<260	<104
J_1+J_2[b]	19 10 14.21	9 06 25.1	6.06	3.8	5.13	0.89	6.40	4.6	238	57.9
JJ	19 10 18.73	9 06 06.3	diffuse	21.5	203	120	diffuse	19.2	764	404
KK	19 10 21.69	9 05 51.5	6.29	10.0	20.9	12.4	6.98	12.3	124	57.7
L	19 10 14.76	9 06 17.0	4″ ring	6.1	24.0	9.43	diffuse	6.1	328	92.7
LL	19 10 22.89	9 04 13.9	diffuse	11.5	33.9	16.4	diffuse	11.5	90.4	80.6
M	19 10 14.73	9 06 25.1	4.06	3.8	8.33	3.24	5.4	3.1	65.1	10.8
MM	19 10 23.56	9 06 02.4	diffuse	19.2	90.4	52.5	diffuse	21.5	416	273
N	19 10 15.38	9 06 14.9	PR	3.1	<5.01	<2.99	4.4	3.1	44.2	4.64
O	19 10 16.33	9 06 06.8	5.4	3.8	8.11	2.79	6.67	3.8	134	87.5
O_2	19 10 16.30	9 06 11.6	PR	3.8	<9.57	<3.60	PR	3.8	<90.7	<66.8
O_3	19 10 17.03	9 06 10.7	4″ ring	7.7	32.4	12.3	4″ ring	7.7	<202	<123
P	19 10 16.90	9 05 52.1	4.59	5.4	11.7	6.02	6.33	5.4	70.3	37.0
Q	19 10 10.65	9 05 05.6	diffuse	7.7	41.4	35.8	diffuse	9.2	246	233
R_{tot}[c]	19 10 10.80	9 05 18.5	6.92	6.9	58.9	47.9	11.5	6.9	485	408
R	19 10 11.06	9 05 20.2	PR	1.5	<2.84	<2.34	PR	1.5	<38.5	<37.0
R_2	19 10 10.80	9 05 23.2	PR	1.5	<1.23	<0.96	PR	1.5	<14.8	<13.3
R_3	19 10 10.74	9 05 17.4	PR	1.5	<7.41	<7.22	PR	1.5	<39.9	<38.3
S	19 10 11.76	9 05 26.6	5.22	6.9	77.4	65.1	7.68	8.4	402	302
W49 South	19 10 22.32	9 05 01.0	5.39	23.0	405	349	6.83	23.0	2290	2150
W49 South-1	19 10 21.60	9 05 01.1	U	1.5	<7.99	<7.88	U	1.5	<69.6	<68.2

Notes. R.A. and decl. are for the center of apertures used, not the source peaks. F_{int} indicates total flux inside the aperture. $F_{int\text{-}bg}$ is for background-subtracted flux. For the columns labeled "FWHM": "ND" means no detection (so the corresponding flux is calculated as a 3σ upper limit from the background), "U" means unresolved from other emission, and "PR" means partially resolved from other emission (so flux values are upper limits due to contamination), "diffuse" means the source is large and cannot be fit by a Gaussian profile, "low S/N" means the detection is too faint to be fit by a Gaussian profile. Some sources are rings or partial rings or arcs and the radius of a ring that fits their shape is given.

[a] G_{tot} here refers to the collective flux of unresolved sources G_1, G_2, G_3, G_4, and G_5.

[b] J_1+J_2 here refers to the collective flux of unresolved sources J_1 and J_2.

[c] R_{tot} here refers to the collective flux of unresolved sources R, R_2, and R_3 from the table above, as well as R_4, which can be found in Table 2.

within an annulus just outside that aperture, the thickness of which is determined by the range of radii where the background remains at a constant level. These background-subtracted flux estimates are given in Table 1 in the columns labeled $F_{int\text{-}bg}$.

If the radial profile can be fit by a Gaussian, we report that value in the FWHM column of Table 1. If we cannot fit a Gaussian profile, a reason is given in the FWHM column. "ND" means it was a nondetection, and a 3σ upper-limit value is given for F_{int} (and no value is given for $F_{int\text{-}bg}$). This only applies to sources A (at 20 and 37 μm) and GG (at 20 μm only). We used the background statistics within an aperture that would fit the radio size of source A (3.″1) centered on the location of the radio source peak to estimate the upper-limit fluxes. "PR" and "U" mean "partially resolved" and "unresolved," respectively. This means there is too much contamination (or variability in the contamination) from nearby sources to estimate a flux density from the source alone. We therefore employed an aperture size for these sources that was either just large enough to contain the radio source extent or

Table 2
Observational Parameters of All Newly Identified Sources in W49A

Source	R.A. J2000	Decl. J2000	20 μm FWHM ($''$)	20 μm R_{int} ($''$)	20 μm F_{int} (Jy)	20 μm F_{int-bg} (Jy)	37 μm FWHM ($''$)	37 μm R_{int} ($''$)	37 μm F_{int} (Jy)	37 μm F_{int-bg} (Jy)
CC-1	19 10 13.76	9 07 20.8	8.15	8.4	12.9	4.94	diffuse	8.4	46.8	22.5
DD-1	19 10 11.34	9 06 20.9	2.42	3.1	1.78	0.20	4.3	3.8	14.5	2.82
II-1	19 10 14.47	9 06 48.3	1.93	4.6	2.93	0.55	3.94	4.6	27.6	6.22
JJ-1	19 10 19.02	9 06 41.7	4.86	9.2	21.4	6.09	10.2	10.0	141	34.3
KK-1	19 10 21.29	9 06 27.6	5.46	3.8	1.45	0.26	4.93	4.6	16.6	7.76
MM-1	19 10 25.43	9 05 43.2	5.61	10.0	19.6	6.02	7.72	10.0	50.9	25.3
P-1	19 10 16.62	9 05 45.5	4.59	3.1	2.55	0.87	4.3	3.1	12.5	5.63
Q-1	19 10 09.93	9 05 09.8	low S/N	3.1	1.03	0.21	low S/N	3.1	6.99	5.58
R_4	19 10 10.92	9 05 16.8	PR	3.1	<25.2	<24.7	PR	3.1	<209	<207
W49 South-2	19 10 21.02	9 05 01.6	low S/N	3.8	2.57	0.49	PR	3.8	<24.7	<22.4

Note. Table note from Table 1 applies here.

was the point-source radius ($1\farcs5$) derived from the average FWHM ($\sim3\farcs1$) at 20 and 37 μm for SOFIA, whichever was larger. The background-subtracted fluxes for unresolved and partially resolved sources are taken from the closest area showing a global minimum (rather than local minimum used for resolved sources) because we cannot determine with any accuracy a good local minimum to use. This means that the F_{int-bg} values in Table 1 are true upper limits to the source fluxes for unresolved and partially resolved sources. If the source is large and flocculent, it is labeled "diffuse." Several sources appear to be wind-blown bubbles or otherwise appear as a ring shape, a broken ring, or a large arc/partial ring. These sources are fit by a circle whose radius best fits the structure, and they are reported in Table 1 with the words "ring" along with the radius value of that fit.

All sources newly identified for the first time in this work, summing 10 new sources in all, are listed in Table 2. The observational parameters listed in that table were obtained in the same way as described in Table 1. Four of these newly identified sources (CC-1, JJ-1, P-1, and R_4) are coincident with radio continuum emission peaks at 3.6 cm, as seen in the maps of De Pree et al. (1997) but were not labeled or discussed in that work, and DD-1 is contained in a region of extended 3.6 cm radio continuum emission with no definitive peak. MM-1 was off field in the available radio data. Four newly identified mid-infrared sources, II-1, KK-1, Q-1, and W49 South-2 have no detected 3.6 cm emission at their locations. In addition to radio source A, some other radio sources identified by De Pree et al. (1997) were not detected in the SOFIA data. Sources B and O_2 were not detected at either SOFIA wavelength as a peak, though there is some diffuse and/or extended mid-infrared emission in their areas. Radio sources C, C_1, D, E, and H may have associated emission at SOFIA wavelengths that is not well resolved from the bright and extended emission of the G complex. Furthermore, compact radio sources GG and N are only clearly detected at 37 μm.

Finally, though we had the sensitivity to detect them, we do not detect mid-infrared emission from previously identified mid-infrared sources BB East, DD South, EE East, and HH West (Smith et al. 2000).

4.1. Physical Properties of Subcomponents and Point Sources: SED Model Fitting and Determining MYSO Candidates

Defining the embedded MYSO population in W49A is one of the primary goals of this study. Thermal infrared observations are able to penetrate through overlying extinction from the larger star-forming cloud complex and are sensitive to the emission from the dust localized near to and enshrouding young and forming stars (or bound star systems). In fact, our previous papers from this GH II region survey (Papers I and II) have shown that, at the SOFIA-FORCAST 20 and 37 μm wavelengths (and $\sim3''$ of angular resolution), we can detect not only the known MYSOs and potential MYSOs within these GH II regions (as found via their free–free radio continuum emission), but we also uniquely find MYSOs in their earliest embedded stages of evolution, prior to the onset of detectable UCH II regions.[3]

In order to identify the MYSO candidates in W49A, we will use SED model fitting. Therefore, the first step is to determine which features in the data are likely to be internally heated sources and measure their flux densities at as many wavelengths as we can to fill out their SEDs. We have already described in the previous section how we performed aperture photometry on our sources. This was performed on the natural resolution images because (as discussed in Section 2) the deconvolved images can be subject to larger flux errors. As a consequence, some groups of sources identified in the three times higher resolution ($0\farcs8$) radio continuum images or partially resolved in our deconvolved SOFIA images are lumped together into a single source if they are not resolved from other nearby sources in the natural resolution SOFIA images (specifically J_1+J_2, G_{tot}, W49 South, and R_{tot}). Source candidates were found as resolved sources or peaks in the 20 and 37 μm natural resolution images, and then cross-referenced with the Spitzer-IRAC, Herschel-PACS, and centimeter radio data for spatial coincidences. Only source candidates that were spatially coincident with sources or emission peaks at longer and/or shorter wavelengths made it to the final source list. In the end, we identified 24 compact infrared sources from the sources in Tables 1 and 2, and they are listed in Table 3. To be considered a "compact" source, the emission had to be compact enough and/or resolved enough from nearby sources to have a measurable FWHM in Tables 1 and 2, though we will additionally include the resolved (yet low-S/N) sources Q-1 and W49 South-2. One needs to note that the far distance of W49A (11.1 kpc) makes it difficult to resolve close binary and

[3] We also can detect lower-mass YSOs that are heavily embedded and possessing stars that are non-ionizing (and thus not detectable in the cm radio continuum).

Table 3
SED Fitting Parameters of Selected Compact Infrared Sources in W49A

Source	L_{obs} ($\times 10^3 L_\odot$)	L_{tot} ($\times 10^3 L_\odot$)	A_v (mag.)	M_{star} ($M_\odot$)	A_v Range (mag.)	M_{star} Range ($M_\odot$)	Best Models	Notes
CC-1	11.6	108	26.5	16	26.5–79.5	12–32	7	MYSO[a]
DD-1	1.77	11.7	68.9	8	33.5–76.8	8–8	8	MYSO
EE	18.0	36.5	72.9	16	10.6–132	12–64	7	MYSO
F	3.53	2.59	26.5	2	12.6–33.5	1–8	10	
G_{tot}	275	841	16.8	64	2.70–92.2	24–96	20	MYSO[a]
GG	39.9	99.2	252	16	252–424	16–24	11	MYSO
I	27.7	41.5	55.6	12	47.7–117	12–24	7	MYSO
II-1	3.59	12.1	23.8	8	23.8–60.4	8–8	6	MYSO
J	37.5	457	101	48	24.3–101	16–96	12	MYSO
J_1+J_2	29.3	2040	233	128	176–233	16–160	7	MYSO
JJ-1	13.4	50.9	53.0	12	13.2–79.5	12–12	10	MYSO
KK	39.8	113	53.0	16	26.5–79.5	12–16	5	MYSO
KK-1	1.17	13.6	36.9	12	23.5–69.6	8–24	6	MYSO[a]
M	5.75	15.3	53.0	8	1.70–53.0	8–32	15	MYSO
MM-1	13.9	20.2	1.70	12	0.80–26.5	12–24	16	MYSO
N	9.54	46.7	218	12	13.2–579	8–128	7	MYSO[b]
O	66.0	119	47.7	24	47.7–53.0	24–24	11	MYSO
P	20.7	549	26.5	48	1.70–28.5	12–48	8	MYSO
P-1	2.53	13.3	53.0	8	26.5–72.9	2–12	25	pMYSO
Q-1	4.06	26.6	127	12	8.40–127	8–12	14	MYSO
R_{tot}	186	2380	33.5	128	17.6–58.7	64–128	7	MYSO
S	175	749	26.5	48	2.70–53.0	24–96	27	MYSO
W49 South	359	1560	16.8	96	2.70–134	32–128	10	MYSO[a]
W49 South-2	20.8	39.94	71.5	12	47.0–79.5	8–16	12	MYSO

Notes. An "MYSO" in the right column denotes an MYSO candidate. A "pMYSO" indicates that there is greater uncertainty in the derived physical parameters and that these sources are possible MYSO candidates.
[a] The SED fits are poor for these sources, likely due to the presence of multiple unresolved sources. However the fits are all under-fitting the data (and therefore underestimating the luminosities), and yet still have luminosities indicative of MYSOs.
[b] Source N has only one nominal data point for the SED fits. However, the fits are somewhat constrained by the Spitzer and Herschel upper limits.

multiple systems since one FORCAST pixel (∼0.″768) corresponds to a spatial size ∼0.04 pc. We also know that several of our "compact sources" contain multiple sources, because of resolution issues. For instance, we do not resolve out radio sources G_1, G_2, G_3, G_4, and G_5 even in the deconvolved SOFIA data, and these sources are treated as a single source G_{tot}. We will discuss more the impacts of multiplicity on our analyses later in this section when we discuss the SED model fitting.

We performed additional aperture photometry for these 24 compact sources with Spitzer-IRAC 3.6, 4.5, 5.8, and 8.0 μm as well as Herschel-PACS 70 and 160 μm archival data. We applied the same photometry methods to the IRAC data as we did to the SOFIA data. Herschel-PACS fluxes for the sources were obtained from the fixed size apertures, i.e., $R_{int} = 5$ pixels for both 70 and 160 μm data, without background subtraction. Following Papers I and II, we consider the Herschel-PACS fluxes as upper limits due to the large and uncertain levels of contamination from the environmental extended emission that makes it difficult to identify the accurate 70 and 160 μm PSFs and flux densities. For some sources either both the 70 μm and seven 160 μm photometry apertures (F, G_{tot}, I, J, KK, and N) or just the 160 μm apertures (EE and M) enclosed saturated pixels. For these sources, we do not include these saturated data points in the SED fitting. We tabulate the Spitzer and Herschel photometry data in the Appendix (Tables 6 and 7, respectively).

To determine how to handle the Spitzer-IRAC photometry data that we would use in our SED model fitting, we first tested the possibility of flux contamination in the 3.6, 5.8 and 8 μm bands due to the presence of emission from polycyclic aromatic hydrocarbons (PAHs) and for contamination in the 4.5 μm band due to shock-excited molecular hydrogen emission by adopting the color–color diagram analysis of Gutermuth et al. (2009) as shown in Figure 11. This analysis finds no "shock-emission-dominant" sources in W49A. For the 12 "PAH emission dominant" sources seen in Figure 11, we defined their IRAC 3.6, 5.8, and 8.0 μm flux densities as upper limits, while the 4.5 μm flux densities were considered as nominal data points.

FORCAST 20 and 37 μm fluxes are assumed to be nominal data points for all sources except GG and N (for which 20 μm measurements are upper limits) and F, J, and W49 South-2 (for which 37 μm measurements are upper limits) due to weak emission and/or strong background emissions. We consider the subtracted background flux of each source and each nominal band flux as the upper-limit error because the total photometric error does not exceed the background flux and the choice of the level of background to subtract off is the highest source of uncertainty. The lower-limit errors of all derived IRAC and FORCAST flux densities are set to the calculated total photometric error, which is estimated to be 20% for all IRAC bands, and 15% and 10% for the FORCAST 20 and 37 μm data, respectively. These flux density uncertainty estimates are consistent with those found in Papers I and II.

We also incorporated the infrared photometry data of Smith et al. (2000) in our SED models for several sources. We only included data from that work for sources with definitive measurements (i.e., no upper limits) and only for the sources

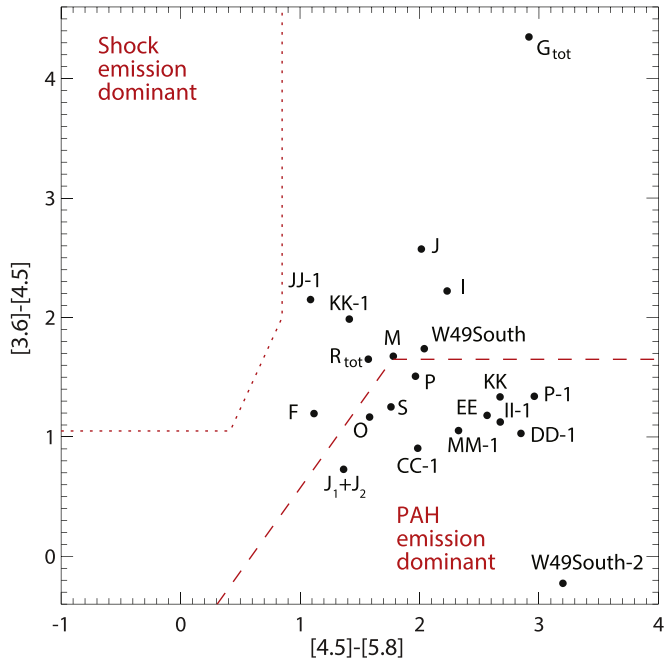

Figure 11. A color–color diagram utilizing our background-subtracted Spitzer-IRAC 3.6, 4.5, 5.8, and 8 μm source photometry to distinguish "shocked emission dominant" and "PAH emission dominant" YSO candidates from our list of subcomponents and point sources. The region above the dotted line (upper left) indicates the shock-emission-dominant regime. The region below the dashed line (bottom right) indicates the PAH-dominant regime. This method was adopted from Gutermuth et al. (2009). Sources GG, N, and Q-1 are not included in this diagram due to weak or nondetection of Spitzer-IRAC bands.

that appear in our Table 3. Explicitly the data included in the fits were for W49 South (at 8.0. 8.6, 9.1, 9.7, 9.8, 10.5, 10.7, 11.3, 12.3, 12.8, 13.2, and 20.6 μm), S (at 10.5, 10.7, 11.3, 12.3, 12.8, 13.2, and 20.6 μm), F, G, I, J, and M (these latter five sources at 12.3, 12.8, 13.2, and 20.6 μm). When comparing the Smith et al. (2000) photometry at 20.6 μm to our SOFIA data at 20 μm, we noticed that the values from Smith et al. (2000) were systematically in between our non-background-subtracted fluxes and our background-subtracted fluxes. For the brighter sources like W49 South, G, and S, the differences between our non-background-subtracted fluxes and our background-subtracted fluxes are small and thus so is the difference of either of these values with those of Smith et al. (2000), i.e., the same to within the combined photometric errors. For the fainter sources, our background-subtracted flux values can be up to half those quoted by Smith et al. (2000). Given that Smith et al. (2000) detected sources that are likely not real (i.e., DD South, EE East, HH West, and BB East), and if this were due to improper background subtraction, the photometry for the rest of the sources could be off as well. It may also be that our method of background subtraction might be oversubtracting flux from the actual sources we are performing photometry on (as we discuss in Section 4). Given that the photometry from Smith et al. (2000) was consistently higher than our photometry at 20 μm, we chose to utilize the data as upper limits only (including their quoted 10% photometric error).

Based on the Spitzer, SOFIA, Herschel, and Smith et al. (2000) photometry and the uncertainties, we constructed near-infrared to far-infrared SEDs of the 24 selected compact sources intending to fit theoretical SED models of MYSOs (Zhang et al. 2013, hereafter ZT models). Each model fit provides normalized minimum χ^2 values (so-called). We selected the group of best-fit models as we did in previous studies (see Papers I and II for details). The number of best-fit models and the ranges of the derived parameters based on the models are listed in Table 3. Figures 12 and 13 show the observed SEDs, and the fits of the best models of the 24 sources are summarized in Table 3.

One obvious issue to address is that the ZT models assume a single central stellar source, and given the extreme distance to W49A, it is highly likely that at least some of our compact sources house multiple unresolved stellar components. It is for this reason that we do not tabulate or discuss the model parameters like disk size or accretion rate, and instead concentrate on the values for internal mass and source luminosity. In Paper I, we showed that the derived stellar masses of a compact source could be trusted even if a SOFIA-defined aperture contained multiple YSOs due to the limited angular resolution of the data. IRS2E in W51A was the representative case. There were four NIR-defined sources (Barbosa et al. 2016) contained within the photometric aperture we used for the 20 and 37 μm data. The stellar mass we derived for IRS2E in Paper I (64 $M_\odot$ for the best-fit model, 64–128 $M_\odot$ for the range) agreed well with the total stellar masses of all four NIR YSOs combined (80 $M_\odot$) as derived by Barbosa et al. (2016). We have a similar case in W49A for source R_{tot}. As seen in Section 3.1.2, R_{tot} contains three different centimeter radio sources identified in De Pree et al. (1997) with a total stellar mass, of 85 $M_\odot$. However, adding the additional radio source that was not identified in that work, R_4 (for which we measure its 3.6 cm flux density to be 9 mJy, which translates into a B0 ZAMS star) adds another $\sim$18 $M_\odot$, for a total of 103 $M_\odot$. The derived stellar mass of the ZT model's best fit is 128 $M_\odot$ with a mass range of 64–128 $M_\odot$ for R_{tot}, which is in fairly good agreement with the estimation from the radio data.

On the other hand, we see in Figures 12 and 13 that there are a few compact sources that are not fit very well with the MYSO models: G_{tot}, W49 South, CC-1, and KK-1. It is likely that these sources are not being fit because they have multiple unresolved MYSOs or stellar sources responsible for their heating, perhaps even at different evolutionary stages or embedded in variable extinction, which would lead to multiple temperature components that could skew the SED data. Source CC-1, in particular, is at the larger end of our "compact" sources size limit, and given its size and relatively bright and extended radio emission, it is very likely excited by more than one massive star. So it could be that the ZT models only do a good job of estimating the overall mass of a binary or protocluster if the sources are coeval or subject to the same extinction (e.g., R_{tot}).

In our previous papers we used the derived data like those compiled in Table 3 to determine which sources are MYSOs or potential MYSO candidates. The conditions for a source to be considered an MYSO candidate in our previous papers has been that it must (1) have an SED reasonably fit by the MYSO models, (2) have an $M_{star} \geqslant 8\,M_\odot$ for the best-fit model, and (3) yield an $M_{star} \geqslant 8\,M_\odot$ in all of the model fits in the group of best-fit models. In those previous papers we categorized "potential MYSOs" (pMYSOs) as sources that fulfilled only the first two of the MYSO criteria. However, as we have been discussing, W49A is so distant compared to those previously observed GH II regions that we are likely seeing some compact sources where multiple stellar components may be affecting the

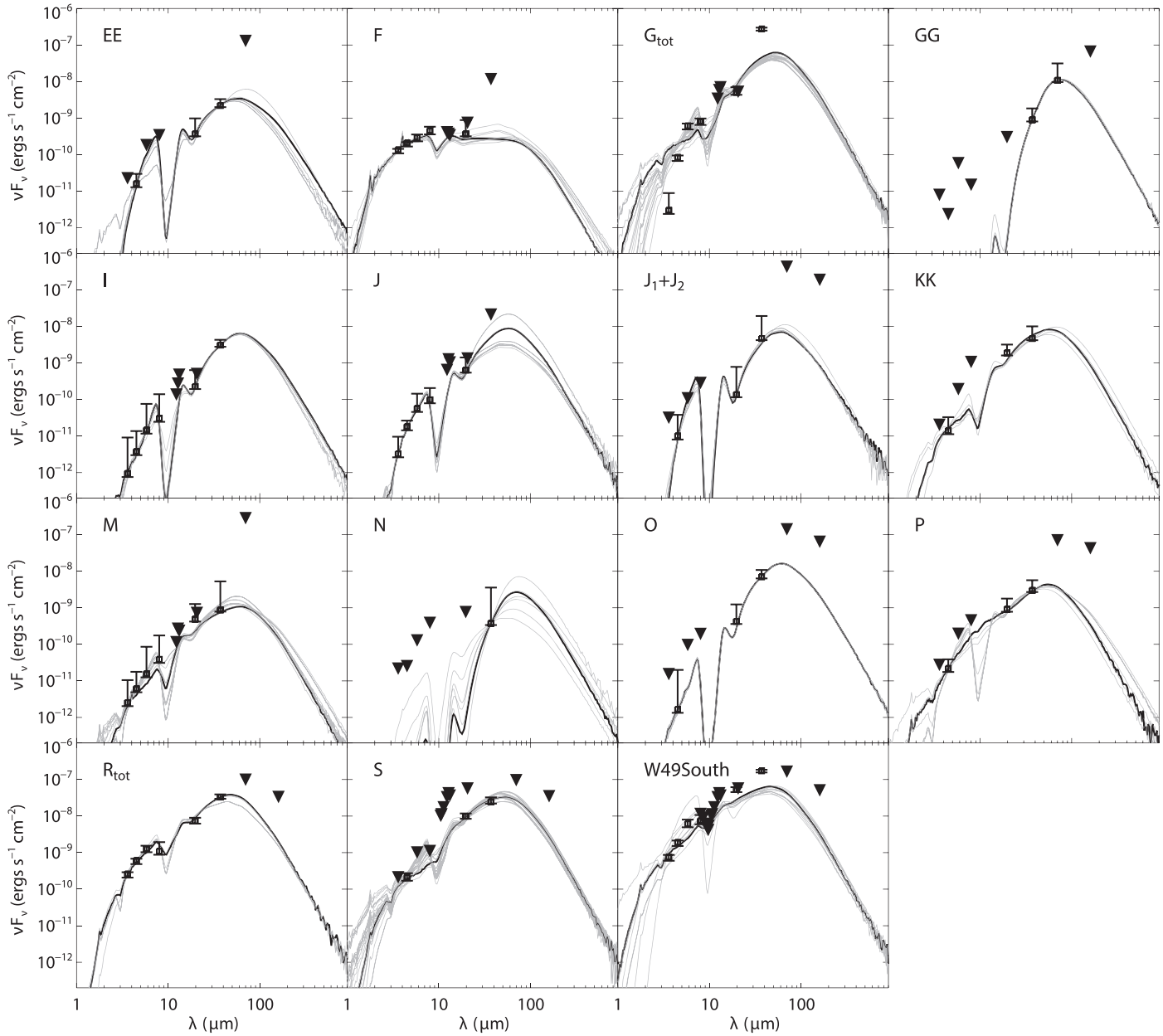

Figure 12. SED fitting with the ZT MYSO models of compact sources in W49A. Black lines are the best-fit model to the SEDs, and the system of gray lines are the remaining fits in the group of best fits (from Table 3). Upside-down triangles are data that are used as upper limits in the SED fits.

SED shape so that they cannot be properly fit by our single-star models. Specifically, G_{tot}, W49 South, CC-1, and KK-1 are not well fit by the MYSO SED models. However, because the best fits to the data for all four sources satisfy criteria (2) and (3) above, and in all four cases the SED fits underfit the data (thus indicating even larger luminosities for these sources than those given in the table), all four sources are likely to contain at least one MYSO.

Because of its great distance and large measured extinction along the line of sight, one would expect that the only YSOs we would be capable of detecting in the mid-infrared would have to be massive. In fact, all sources we identify in Table 3 have an associated 3.6 cm continuum emission (a potential indicator of a possible ionizing MYSO) except for II-1, KK-1, Q-1, and W49 South-2. However, the SED model fitting for all of these sources yields derived luminosities of MYSOs. Therefore, given their lack of radio continuum emission and high luminosities, II-1, KK-1, Q-1, and W49 South-2 are the only MYSOs in Table 3 that could potentially be in an extremely young evolutionary phase prior to the onset of a H II region.

P-1 is the only source that fulfills the pMYSO criteria. It is well fit by the MYSO SED models, and the best fit is for a massive star ($8\,M_{\odot}$), but the range of best fits includes stellar masses less than $8\,M_{\odot}$. Of all of the sources in Table 3, the derived values for source N should be viewed with healthy skepticism as the fits are to data with only one nominal data point (i.e., the SOFIA 37 μm data point). The SED fits are still somewhat constrained by the large number of upper limits at shorter and longer wavelengths; however, the derived values from the group of best fits given in Table 3 vary the most for source N than all others (especially the A_V range). Even with these loose constraints, however, all fits are indicating that the

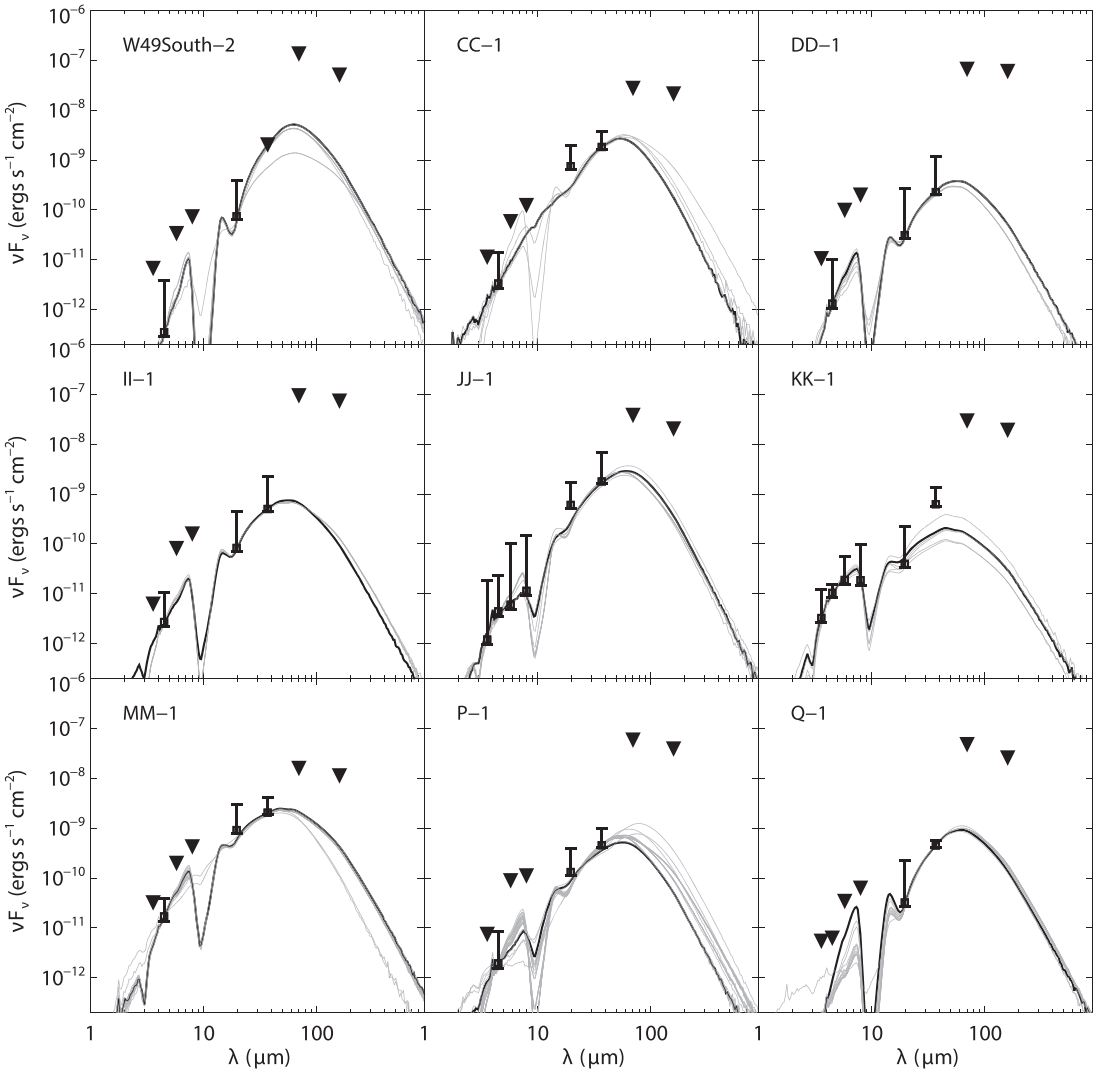

Figure 13. Same as Figure 12 but for newly identified sources in this study.

source contains an MYSO (as would be expected for sources that are only seen at 37 μm and longer wavelengths).

Source F is a special case where it is well fit by the ZT models, and the best-fit mass is only 2 $M_{\odot}$, and it has models that fit only up to 8 $M_{\odot}$. Therefore, source F would not qualify as an MYSO or pMYSO given our above criteria. Interestingly, source F is the least luminous source in our list, yet based on its centimeter continuum flux it is estimated to be ionized by an O7.5 star (De Pree et al. 1997). However, given the 1.3 and 3.6 cm radio fluxes from De Pree et al. (1997), we calculate a radio spectral slope of $\alpha_{\rm radio} = -0.22$, which is atypical for a UCH II region and more indicative of synchrotron emission arising in shocks resulting from the interaction of a collimated stellar wind with a surrounding magnetized medium (e.g., see IRAS 16547–4247 from Garay et al. 2003). Therefore, F may be a less-massive YSO with nonthermal radio centimeter continuum emission coming from a jet/outflow. Interestingly, all sources on the eastern side of the Welch Ring (sources F, H, I, J, J_2, and M) have very negative radio spectral slopes ($-0.22 > \alpha_{\rm radio} > -0.76$), indicating their emissions are dominated by synchrotron emission.[4] Taking all of the above into account, we show in the last column of Table 3 our estimates for which sources we believe are MYSO and pMYSO candidates. The only source with not enough evidence to be categorized as either an MYSO or pMYSO is source F.

In this study, therefore, we classify 22 sources satisfying our criteria of housing an MYSO out of the 24 SOFIA-FORCAST–defined compact sources. Overall, we determined 23 sources to be either an MYSO or pMSYO (∼96%). In Papers I and II, 87% of the point sources were found to likely be MYSOs or pMYSOs in the W51A region ($d \sim 5.4$ kpc), while M17 ($d \sim 2.0$ kpc) showed only 44% sources as MYSOs and pMYSOs. The main reason for the difference was suggested to be the results of the distance of W51A and M17 so that more low- to intermediate-mass YSOs could be detected in M17 due to its relatively closer distance. W49A is about two times farther than W51A from the Sun, and we are measuring an even higher rate of MYSO detection from the SOFIA-FORCAST mid-infrared imaging. More interesting, however, is the drop in the rate of detection of pre-UCH II region MYSOs between the W51A study and this one. Almost half of the sources determined to be MYSOs for W51A have no detectable radio continuum emission, whereas that is the case for only four MYSOs (II-1, KK-1, W49 South-2, and Q-1) in this W49A study. Again, this is likely to be due to the

[4] Sources dominated by thermal bremsstrahlung emission have radio spectral indices of $\alpha_{\rm radio} \geqslant -0.1$, while nonthermal sources dominated by synchrotron emission have $\alpha_{\rm radio} > -0.1$ (Purser et al. 2016).

differences in distance. Pre-UCH II region sources will be compact and are usually found close to other radio-emitting and/or mid-infrared-emitting MYSOs, and thus we are less likely to resolve them from their neighbors at the distance of W49A. Also, not only is there a larger amount of interstellar extinction in the general case of comparing a region 5 kpc away to one 11 kpc away, but in the particular case of W49A, we have the obscuring dust of the Milky Way's Sagittarius spiral arm, which crosses the line of sight to W49A twice. This interstellar and spiral arm extinction heavily affects the transmission of infrared emission from sources within W49A but does not really affect the centimeter radio continuum emission from those same sources. Therefore, this is the likely reason we are mainly detecting the larger, radio-continuum emitting sources of W49A with our SOFIA data.

4.2. Physical Properties of Extended Sources: Kinematic Status and Global History

4.2.1. The Relative Evolutionary States of the Subregions of W49A

In Papers I and II, we compared two independent tracers of molecular clump evolution, the virial parameter ($\alpha_{\rm vir}$) and the luminosity-to-mass ratio (L/M), of the larger extended subregions in W51A and M17. We assume these large and extended radio continuum subregions are candidates for being star-forming clumps (rather than individual cores) housing embedded (proto)clusters of massive stars that are ionizing the extended H II regions seen in the radio continuum. The higher $\alpha_{\rm vir}$ and L/M values are assumed to demonstrate relatively older proto/young stellar clusters, and plotting the $\alpha_{\rm vir}$ versus L/M parameters for these sources in W51A and M17 yielded a relatively linear correlation. We repeated this same analysis here, this time toward the radio-defined extended sources of W49A.

We identified 15 extended radio continuum regions throughout W49A by identifying separate regions in the 37 and 70 μm maps that correlate with the major radio continuum regions identified by De Pree et al. (1997) in their 3.6 cm map. As seen in Figure 14, separate regions identified in the radio continuum maps do not always appear as separate sources in the infrared. We thus had to group some closely positioned radio continuum sources/regions into one region for study. In most cases, these radio regions do share a common diffuse radio continuum envelope as seen in the 3.6 cm map (i.e., Figure 2(a)). Specifically, we group most of the western Welch Ring sources into one source called the "G Region," we group together the bright L and M sources into the "L + M Region," all of the O sources (i.e., O, O_2, and O_3) into the "O Region," and the R and Q complexes into the "R + Q Region." We tabulate the observational parameters from the SOFIA data for the major subregions within W49A in Table 4. For all extended sources, the value of the aperture to use for the photometry was determined by looking at the centimeter radio maps and finding an aperture that encompasses all of the centimeter emission from each source as well as the extended dust emission as seen in the SOFIA 20 and 37 μm maps and determining the smallest aperture radius that would encompass each source at all of these wavelengths. These radii were used for all photometry performed on data at SOFIA and Spitzer wavelengths (i.e., $R_{\rm int}$ in Tables 4 and 8). Descriptions of how we determine the apertures for each source in the Spitzer and Herschel data are detailed in Appendix B.

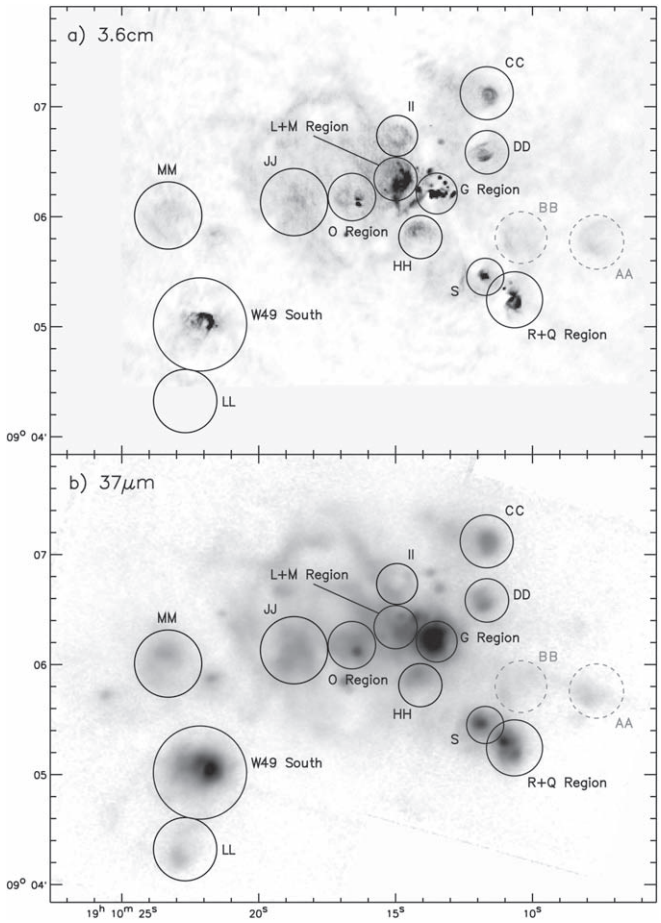

Figure 14. The major radio-defined subregions within W49A. Labeled in black are the sources chosen for the extended region analyses. The circles are demonstrating the size and positions of the apertures used for photometry of the extended regions, as given in Table 4. Sources AA and BB are shown here in gray for completeness, but they are likely not star-forming clumps. (a) 3.6 cm radio map from De Pree et al. (1997). (b) The 37 μm SOFIA map.

To perform our evolutionary analyses, first the masses of each major extended region were derived based on the pixel-by-pixel graybody-fitting method of Lim et al. (2016) where the far-infrared data from Herschel and JCMT were used to determine the cold dust components. Then the bolometric luminosities, L, for these extended sources were calculated based on a two-temperature graybody fit with the integrated total fluxes of each source and each band (see Table 4, as well as Appendix B). For both graybody-fitting methods, the background fluxes of well-resolved extended sources (filled circles of Figure 15) were estimated from the immediate outer annuli of each source. For sources that were not well resolved or displayed strong nearby environmental emission, we calculated the background fluxes based on an average from representative areas in the center of W49A that were relatively free of bright source emission. Because the background subtraction and, thus, parameters derived from their fluxes are less certain for these sources, we plot them with a different symbol (open circles) in Figure 15. Also, following the techniques of our previous papers, we utilized the ^{13}CO(1–0) data of FOREST Unbiased Galactic plane Imaging survey with the Nobeyama 45 m telescope (FUGIN; Umemoto et al. 2017) in order to derive the kinematic property, $\alpha_{\rm vir}$, for each of these extended sources. We summarize in Table 5 the physical parameters we derived for each extended source under the

Table 4
Observational Parameters of Major Subregions within W49A

Source	R.A. J2000	Decl. J2000	R_{int} ($''$)	20 μm F_{int} (Jy)	20 μm F_{int-bg} (Jy)	37 μm F_{int} (Jy)	37 μm F_{int-bg} (Jy)
AA	19 10 07.6	9 05 45.6	15.0	33.5	9.57	106	58.4
BB	19 10 10.4	9 05 47.7	14.2	36.2	8.93	165	50.3
CC	19 10 11.6	9 07 07.8	14.5	112	74.8	385	246
DD	19 10 11.6	9 06 35.1	12.0	58.5	29.3	280	147
G Region	19 10 13.4	9 06 12.6	11.2	72.7	44.7	4110	3720
HH	19 10 14.0	9 05 48.6	12.0	52.5	17.8	369	168
II	19 10 14.9	9 06 44.7	11.1	32.1	1.56	286	41.9
JJ	19 10 18.7	9 06 07.8	18.6	228	123	992	417
L + M Region	19 10 15.0	9 06 20.7	11.9	75.4	23.6	968	338
LL	19 10 22.7	9 04 19.2	17.5	70.6	21.1	189	98.7
MM	19 10 23.3	9 06 00.6	18.5	119	51.0	505	283
O Region	19 10 16.6	9 06 10.8	13.1	96.7	33.7	724	390
R + Q Region	19 10 10.6	9 05 14.7	15.4	127	96.2	903	776
S	19 10 11.7	9 05 27.0	10.2	95.9	70.6	493	305
W49 South	19 10 22.1	9 05 01.1	25.5	445	350	2440	2180
W49 Southwest[a]	19 10 11.28	9 05 15.6	21.5	223	180	1420	1280
W49 North[a]	19 10 15.94	9 06 30.8	69.0	1190	812	11500	10100

Notes. R.A. and decl. are for the center of apertures used, not the source peaks. R_{int} gives the size of the radius used for aperture photometry. F_{int} indicates the total flux inside the aperture. F_{int-bg} is for background-subtracted flux.
[a] W49 North and W49 Southwest are not used in the extended region analyses but are included here for completeness. W49 Southwest is the combined S, R, and Q regions. W49 North is basically the entire central region of W49A, not including W49 Southwest or W49 South.

assumption that they are each a star-forming clump, i.e., the virial mass (M_{vir}), clump mass (M), bolometric luminosity (L), the derived warm and cold temperature components (T_{cold} and T_{warm}), the luminosity-to-mass ratio (L/M), and the virial parameter (α_{vir}).

As shown in Table 5, the extended sources in W49A have masses spanning from 622 $M_\odot$ to 5760 $M_\odot$ while the mean mass, $\overline{M}$, is ~1636 $M_\odot$. For comparison, the $\overline{M}$ of both M17 and W51A are larger at ~2100 $M_\odot$ and ~3500 $M_\odot$, respectively. Furthermore, the mass range of the extended sources in M17 (~20 $M_\odot < M <$ 4340 $M_\odot$) skews lower than W49A, while the W51A mass range skews higher (~107 $M_\odot < M <$ 9930 $M_\odot$). Additionally, the mass range of extended sources in W49A also has less scatter than M17 and W51A, with a standard deviation of the clump masses of only ~1378 $M_\odot$ (compared to ~2090 $M_\odot$ for M17 and ~3510 $M_\odot$ for W51A).

The level of the kinematic stability within GH II regions can be inspected via virial analysis of the individual extended sources they contain. For instance, in Paper I, we derived the α_{vir} values for 13 radio-defined extended sources in W51A. The calculated values of α_{vir} derived for W51A spanned a range between 0.18 and 12.5. We found eight of them are gravitationally bound ($\alpha_{vir} < 2$) while six of them were self-collapsing ($\alpha_{vir} < 1$). The other five sources were extremely unbound ($\alpha_{vir} \gg 2$). The large variation of these α_{vir} values for W51A indicates that multigenerational star formation is occurring within the GH II region, consistent with results from previous studies. Similarly, the extended sources in M17 also showed a large spread of α_{vir} spanning from 0.29 to 9.56. However, as we can see from Table 5, W49A has an α_{vir} range between 0.8 and 3.8, where only two subregions (the G Region and JJ) have a value of $\alpha_{vir} < 1$ consistent with presently undergoing self-gravitational collapse. Three sources (LL, W49 South, and the L+M Region) are expanding but still gravitationally bound ($2 > \alpha_{vir} > 1$), and all of the other sources appear to be gravitationally unbound ($\alpha_{vir} > 2$). However, we caution against overinterpretation of the data in the case of W49A, as even the subregion with the highest virial parameter (i.e., $\alpha_{vir} = 3.8$) is within the estimated factor of 2 error (see the error bar in Figure 15) of being gravitationally bound (i.e., $\alpha_{vir} < 2$). This again is in contrast to our results of W51A and M17, which showed extended subregions with α_{vir} values firmly categorized as self-collapsing even when taking into account the factor of 2 error (i.e., having $\alpha_{vir} < 0.5$) and firmly categorized as gravitationally unbound (i.e., having $\alpha_{vir} > 4$).

Although the virial analysis tentatively shows the evolution and the kinematic state of each molecular clump simultaneously, the L/M would show the evolutionary state of the clump only (e.g., Krumholz & Tan 2007). Excluding extended radio regions AA and BB (because our L/M analysis only holds for star-forming clumps; see Section 3.1.6), the minimum and maximum L/M values of the extended sources in W49A are 83 $L_\odot/M_\odot$ and 540 $L_\odot/M_\odot$, respectively. For comparison, W51A and M17 showed the ranges $26 \lesssim L/M \lesssim 800\, L_\odot/M_\odot$ and $300 \lesssim L/M \lesssim 2000\ L_\odot/M_\odot$, respectively. Note that Ma et al. (2013) inspected the L/M of the 303 mid- to high-mass star-forming clumps of the Milky Way from their unbiased CO surveys where the clumps showed $0.1 \lesssim L/M \lesssim 1000 L_\odot/M_\odot$ across entire evolutionary states.

As we did in our previous studies, we plot the α_{vir} versus L/M for the star-forming clumps in W49A in Figure 15 where we place the clumps of W51A and M17 as well. The plot clearly shows that the relative age spread of the clumps in W49A is smaller than in the W51A and M17 cases. It also shows that the clumps in W49A tend to be missing an extremely young (i.e., sources in the lower left of the plot) population compared to W51A and M17. The small overall spread in the data points on this plot appears to indicate the star-forming clumps in W49A tend be more coeval, unlike the cases of W51A and M17.

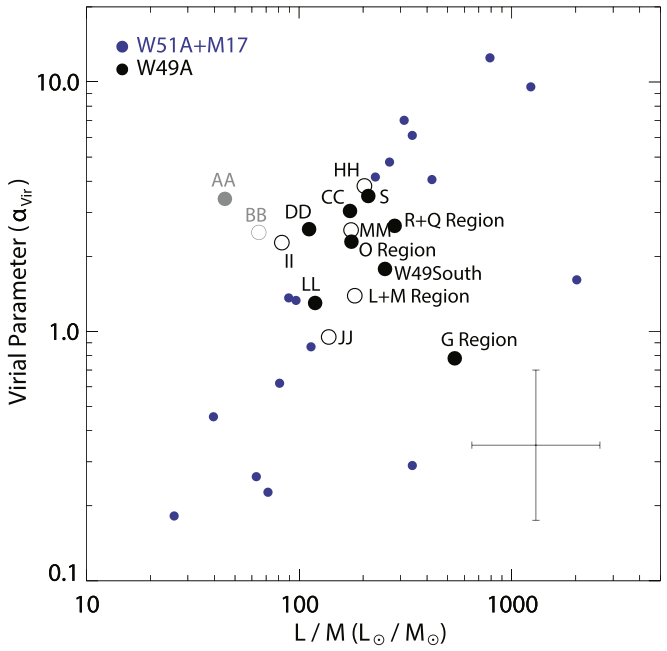

Figure 15. $\alpha_{\rm vir}$ vs. L/M of extended sources in W49A. L/M is calculated based on the infrared data where the background levels are determined from the outer annuli of individual sources for the filled circles. Backgrounds of open circles are estimated from the central region of W49A. Sources AA and BB are shown here in gray for completeness, but they are likely not star-forming clumps.

However, there is one source in Figure 15 that stands out. The source with the lowest virial parameter, the G region, contradictorily has the highest L/M value. Consistent with its low virial parameter value, the G region is very likely a youthful region, given that it is in the area of highest extinction in W49A and houses the highest concentration of MYSOs in the entire GH II region. The other two blue points on the graph in the lower right that accompany the G region are the northern and southern bar sources of M17. Our conjecture for M17 is that these regions are further subject to intense external heating and ionization that could skew the L/M values higher than expected for a self-luminous source alone. This could be the case with the G region of W49A, because it is located in an area with the highest level of environmental radio continuum emission.

4.2.2. The History of Stellar Cluster Formation in W49A

There have been many studies looking into how star formation proceeded within W49A, with contradictory conclusions. Alves & Homeier (2003) and Homeier & Alves (2005) used a near-infrared color–color diagram analysis to deduce the relative age distribution of the stellar clusters and UCH II regions and concluded that W49A experienced independent multiseeded star formation activities. Based on the expansion ages of the UCH II regions within W49A, Conti & Blum (2002) suggested that the star formation of W49A started from the periphery then moved to the central region (i.e., the Welch Ring). Peng et al. (2010), however, suggested expanding shells centered within the Welch ring triggered the star formation in the other regions of W49A so that the direction of the sequential star formation would be opposite to what Conti & Blum (2002) suggested. Rugel et al. (2019) studied the kinematic properties of the radio recombination lines (as part of the THOR survey; Wang et al. 2018) in W49A and concluded that it has undergone expanding and recollapsing events where these events formed multiple generations of young stellar clusters. It is worthy to note that they claimed the relative ages among the different generations of the stellar clusters were very small.

In Paper I, we suggested that the sequentially triggering star formation would be easily recognized in the $\alpha_{\rm vir}$ versus L/M plot with a simple linear correlation so that the younger clumps/clusters are located at the lower left (low $\alpha_{\rm vir}$ and L/M) and the older ones would be opposite. Then by inspecting how these young and old regions are distributed within the GH II region one could speculate as to whether the data are consistent with triggering scenarios or not. As shown in Figure 15, the data points for the subregions in W49A do not extend to the very young or very old corners of the plot but are instead grouped fairly tightly together near the center of the plot. This seems to indicate that, globally, the star-forming subregions within W49A are relatively coeval given the small spread in both evolutionary indicators, L/M and $\alpha_{\rm vir}$. This implies nonsequentially triggered, multiseeded star formation activity throughout W49A, as suggested by Alves & Homeier (2003) and Homeier & Alves (2005). The coeval nature of all extended subregions in W49A would be inconsistent with sequentially triggered (i.e., longer timescale) formation scenarios like both the outside-in formation scenario (i.e., Conti & Blum 2002) and the inside-out formation scenario (i.e., Peng et al. 2010).

There is an additional origin scenario that states the global star formation throughout W49A might have been initiated by a cloud–cloud collision occurring along our line of sight to the region. This scenario was originally suggested by Mufson & Liszt (1977) based on molecular and recombination line observations, with follow-up studies supporting the idea (e.g., Serabyn et al. 1993; Buckley & Ward-Thompson 1996). Unfortunately, our data cannot prove such a scenario, and more direct evidence of the cloud–cloud collision scenario will need targeted observations, such as comparing velocity profiles of the 158 μm [C II] line emission and CO isotopologue bands (Bisbas et al. 2018; Lim et al. 2021). However, such a global triggering scenario could explain why so many subregions spread throughout such a large volume could have begun star formation activities at the same time.

5. Summary

In this, our third paper from our mid-infrared imaging survey of Milky Way GH II regions, we obtained SOFIA-FORCAST 20 and 37 μm maps toward W49A, covering the entire infrared-emitting area of the region at $\sim$3″ spatial resolution. The 37 μm images are the highest spatial resolution infrared observations of W49A yet obtained at wavelengths beyond 25 μm. We compared these SOFIA-FORCAST images with previous multiwavelength observations from the near-infrared to radio wavelengths from various ground- and space-based telescopes in order to inspect the morphological and physical properties of the compact and extended sources within in W49A. We itemize below our main conclusions from this study.

(1) The infrared observations from SOFIA show the region to have structured but extended dust emission spread over a $\sim 5\farcm0 \times 3\farcm5$ area, which corresponds generally to the extent of the centimeter radio continuum emission seen by De Pree et al. (1997). While most of the infrared

Table 5
Derived Parameters of Major Subregions in W49A

Source	M_{vir} ($M_\odot$)	M ($M_\odot$)	L ($\times 10^4 L_\odot$)	T_{cold} (K)	T_{warm} (K)	L/M $L_\odot/M_\odot$	α_{vir}
AA	2312.70	679.20	6.1	55.5	272.6	*44.8*[a]	3.4
BB	3061.80	1245.70	16.1	43.3	297.1	*64.7*[a]	2.5
CC	2323.70	763.80	26.5	61.4	269.8	173.6	3.0
DD	2252.90	875.40	19.5	54.7	266.1	111.5	2.6
G Region	4477.10	5760.50	622.0	71.4	245.3	539.5	0.8
HH	3092.80	807.90	32.8	47.3	260.0	202.9	3.8
II	3674.70	1621.60	26.9	38.4	365.7	83.0	2.3
JJ	2374.30	2510.30	68.8	53.3	252.4	137.0	0.9
L + M Region	3151.00	2266.10	82.8	48.0	282.2	182.8	1.4
LL	1056.30	813.30	19.4	47.5	262.6	119.0	1.3
MM	2107.30	826.50	28.8	58.9	261.8	174.6	2.5
O Region	3341.40	1459.50	51.5	54.8	282.7	176.3	2.3
R + Q Region	2796.20	1053.60	59.3	74.8	296.0	281.6	2.7
S	2174.70	622.30	26.3	82.3	261.6	211.5	3.5
W49South	5777.70	3241.60	164.0	78.9	271.9	253.6	1.8

Note.
[a] As discussed in Section 3.1.6, AA and BB are likely not star-forming clumps. Because the L/M analysis only holds for star-forming clumps, these values do not accurately represent the evolutionary state of these sources.

features are resolved at both SOFIA wavelengths, the dust is more pronounced and extended at 37 μm compared to 20 μm, indicative of widespread cool dust.

(2) The most well-known feature in W49A is the ring of radio continuum sources referred to as the Welch Ring. We do not detect 20 μm emission coming from the locations of radio sources on the western side of this ring, namely sources A, B, B_1, D, or E. However, in the deconvolved 37 μm image there is extended emission toward the locations of B_1, D, and E, and while it is possible that this is simply unresolved emission from the very bright G source, contributions to the emission in these areas due to sources B_1, D, and/or E cannot be ruled out. It is presumed that the reason for the nondetections in the infrared is because the extinction is higher on the western side of the ring of radio sources. We determined the radio spectral slope of the Welch Ring radio sources and discovered several of the sources in the eastern side have radio emission indicative of nonthermal synchrotron emission (likely from ionized jets/outflows), rather than free–free bremsstrahlung emission from UCH II regions.

(3) The two sources with the largest derived luminosities are W49 South and source G. W49 South is the brightest peak in all of W49A in the infrared from ~3 μm out to ~20 μm. However, our data show that at 37 μm and longer wavelengths (as seen by Herschel) it becomes the second brightest peak to source G. This suggests that, while both contain young MYSOs, G is likely at a relatively earlier and more embedded phase of evolution.

(4) We have identified 10 new sources from the SOFIA data: CC-1, DD-1, II-1, JJ-1, KK-1, MM-1, P-1, Q-1, R_4, and W49 South-2.

(5) Though we had the sensitivity to detect them, we do not detect mid-infrared emission from previously identified mid-infrared sources BB East, DD South, EE East, and HH West (Smith et al. 2000). These sources are also not seen in the Spitzer-IRAC data and therefore might not be real sources.

(6) Radio sources AA and BB are large ($d > 1$ pc), extremely diffuse radio continuum regions with faint ring or bubble-like appearances, relatively low infrared-derived luminosities, and possess the lowest radio emission measures of any subregion within W49A. They both have a stellar source centrally located within their extended radio continuum regions, which may be singularly responsible for their ionization. We suggest that, based upon these data, AA and BB are evolved H II regions and not star-forming subregions.

(7) We performed SED modeling on 24 identified compact infrared sources using photometry of SOFIA, Spitzer, and Herschel data. We found 22 sources satisfying our criteria of housing an MYSO, and we determined 23 sources to be either an MYSO or pMSYO (~96%). In our two previously studied GH II regions, 87% of the point sources were found to likely be MYSOs or pMYSOs in the W51A region ($d \sim 5.4$ kpc), while M17 ($d \sim 1.98$ kpc) showed only 44% sources as MYSOs and pMYSOs. We suggest that the main reasons for detecting such a high fraction of MYSOs with SOFIA are due to the combination of the much larger extinction toward W49A and its extreme distance (11.1 kpc), which would make less-massive (and therefore less luminous) YSOs difficult to detect.

(8) While almost half of the sources determined to be MYSOs for W51A have no detectable radio continuum emission, that is the case for only four MYSOs (II-1, KK-1, Q-1, and W49 South-2) in this W49A study. This is likely a consequence of the much larger distance and extinction toward W49A.

(9) It has been speculated that W49A may be a relatively young GH II region overall (Welch et al. 1987). Our evolutionary analyses show that W49A appears to be absent of an extremely young population compared to W51A and M17. This appears to indicate that W49A is neither an extremely young or old GH II region globally. Our evolutionary analyses also show that the relative age spread of the star-forming clumps in W49A is smaller

than the W51A/M17 cases, and thus are much more coeval. This coeval nature of the extended subregions in W49A is inconsistent with internally triggered, sequential formation scenarios and may be more consistent with a single global triggering event.

This research is based on observations made with the NASA/DLR Stratospheric Observatory for Infrared Astronomy (SOFIA). SOFIA is jointly operated by the Universities Space Research Association, Inc. (USRA), under NASA contract NAS2-97001, and the Deutsches SOFIA Institut (DSI) under DLR contract 50 OK 0901 to the University of Stuttgart. This work is also based in part on archival data obtained with the Spitzer Space Telescope, which is operated by the Jet Propulsion Laboratory, California Institute of Technology under a contract with NASA. This work is also based in part on archival data obtained with Herschel, a European Space Agency (ESA) space observatory with science instruments provided by European-led Principal Investigator consortia and with important participation from NASA. Financial support for this work was provided by NASA through SOFIA awards 05_0008 and 06_0011 issued by USRA.

Facility: SOFIA(FORCAST).

Appendix A
Data Release

The FITS images used in this study are publicly available at https://dataverse.harvard.edu/dataverse/SOFIA-GHII.

The data include the SOFIA-FORCAST 20 and 37 μm final image mosaics of W49A and their exposure maps.

Appendix B
Additional Photometry of Compact and Extended Sources in W49A

In addition to the fluxes derived from the SOFIA-FORCAST data, we used some additional photometry data in our SED analyses from Smith et al. (2000), as well as measured fluxes for our sources from both Spitzer-IRAC and Herschel-PACS.

B.1. Compact Sources

As mentioned in Section 4, we performed optimal extraction photometry for the FORCAST 20 and 37 μm images to define the location of all compact sources and to determine the aperture radii to be used for photometry. Using these source locations, we employed the optimal extraction technique on the Spitzer-IRAC 8 μm data for all sources to find the optimal aperture to be used for all IRAC bands (because the source sizes are typically similar or smaller at the shorter IRAC bands). As we have done for the FORCAST images, we estimated the background emission from the annuli that showed the least contamination from nearby sources, i.e., showing a relatively flat radial intensity profile (Section 4). Table 6 shows the photometry values we derive for all compact sources from the Spitzer-IRAC bands.

Table 7 shows the photometry result for the Herschel-PACS bands for the compact sources. In general, this aperture size cannot be determined accurately using the optimal extraction technique due to the ubiquity of extended emission from nearby sources that are overlapping the source being measured. Indeed, only one compact source (GG) could be resolved in PACS band images, so for all other sources, we use fixed aperture radii for both PACS bands ($R_{\rm int} = 16.''0$ for 70 μm and

Table 6
Spitzer-IRAC Observational Parameters of Compact Sources in W49A

Source	$R_{\rm int}$ ($''$)	3.6 μm		4.5 μm		5.8 μm		8.0 μm	
		$F_{\rm int}$ (Jy)	$F_{\rm int\text{-}bg}$ (Jy)	$F_{\rm int}$ (Jy)	$F_{\rm int\text{-}bg}$ (Jy)	$F_{\rm int}$ (Jy)	$F_{\rm int\text{-}bg}$ (Jy)	$F_{\rm int}$ (Jy)	$F_{\rm int\text{-}bg}$ (Jy)
CC-1	2.4	0.0134	0.0034	0.0206	0.0050	0.1117	0.0199	0.3242	0.0678
DD-1	3.0	0.0125	0.0012	0.0150	0.0020	0.1883	0.0175	0.5248	0.0581
EE	4.8	0.0271	0.0127	0.0447	0.0241	0.3525	0.1637	0.9083	0.3928
F	3.0	0.1731	0.1626	0.3301	0.3130	0.6908	0.5603	1.5504	1.1992
$G_{\rm tot}$	2.4	0.0107	0.0036	0.1424	0.1259	1.3734	1.1827	2.5986	2.1640
GG	3.8	<0.0095	⋯	<0.0035	⋯	<0.1130	⋯	<0.0400	⋯
I	2.4	0.0110	0.0011	0.0205	0.0056	0.1467	0.0281	0.3718	0.0816
II-1	3.6	0.0074	0.0023	0.0160	0.0041	0.1559	0.0307	0.4208	0.0756
J	2.4	0.0115	0.0039	0.0397	0.0269	0.2782	0.1100	0.5491	0.2624
J_1+J_2	4.2	0.0380	0.0120	0.0570	0.0150	0.2083	0.0339	0.7562	0.0988
JJ-1	3.0	0.0222	0.0014	0.0342	0.0067	0.2004	0.0117	0.3876	0.0306
KK	3.6	0.0243	0.0096	0.0493	0.0210	0.3705	0.1581	2.8366	0.7992
KK-1	2.4	0.0147	0.0039	0.0235	0.0156	0.1106	0.0367	0.2560	0.0500
MM-1	6.0	0.0381	0.0151	0.0592	0.0255	0.3799	0.1392	1.1234	0.4616
M	2.4	0.0126	0.0031	0.0265	0.0091	0.1657	0.0302	0.4667	0.1035
N	3.0	<0.0260	⋯	0.0379	0.0025	0.2467	0.0058	<1.0296	⋯
O	2.4	0.0184	0.0013	0.0300	0.0025	0.1854	0.0069	0.5129	0.0091
P	3.6	0.0330	0.0128	0.0584	0.0328	0.3758	0.1286	1.2071	0.5455
P-1	2.4	0.0089	0.0013	0.0126	0.0029	0.1701	0.0286	0.2934	0.0367
Q-1	2.4	<0.0065	⋯	<0.0093	⋯	0.0654	0.0044	0.1663	0.0085
$R_{\rm tot}$	3.6	0.3491	0.3108	1.0205	0.9094	2.9816	2.4747	5.1631	2.9199
S	4.8	0.2527	0.1573	0.4104	0.3186	1.9483	1.0326	2.9391	1.2742
W49 South	16.2	1.0395	0.8972	3.2082	2.8473	15.4830	11.9295	28.5123	19.7979
W49 South-2	1.8	0.0080	0.0010	0.0058	0.0005	0.0645	0.0065	0.1929	0.0442

Table 7
Herschel-PACS Observational Parameters of Compact Sources in W49A

Source	70 μm		160 μm	
	R_{int} ($''$)	F_{int} (Jy)	R_{int} ($''$)	F_{int} (Jy)
CC-1	16.0	633	22.5	1120
DD-1	16.0	1528	22.5	3166
EE	16.0	3016	22.5	…
F	16.0	…	22.5	…
G_{tot}	16.0	…	22.5	…
GG	9.6	252[a]	22.5	3524
I	16.0	…	22.5	…
II-1	16.0	2180	22.5	3890
J	16.0	…	22.5	…
J_1+J_2	16.0	…	22.5	…
JJ-1	16.0	879	22.5	1076
KK	16.0	…	22.5	…
KK-1	16.0	679	22.5	1011
M	16.0	6587	22.5	…
MM-1	16.0	367	22.5	595
N	16.0	…	22.5	…
O	16.0	3261	22.5	3413
P	16.0	1633	22.5	2263
P-1	16.0	1356	22.5	2058
Q-1	16.0	1103	22.5	1357
R_{tot}	16.0	2302	22.5	1776
S	16.0	2239	22.5	1861
W49 South	16.0	3815	22.5	2688
W49 South-2	16.0	3110	22.5	2674

Note.
[a] F_{int-bg} (nominal data point) because source GG could be resolved in the PACS 70 μm map. The F_{int} of 70 μm is 731.86 Jy.

$R_{int} = 22.''5$ for 160 μm). We compared our aperture sizes to those typically used in the Hi-GAL Compact Source Catalogue (Molinari et al. 2016; Elia et al. 2017). That catalog employs aperture sizes comparable to the ones we used in this study. We therefore believe that the fixed aperture sizes we employ here are reasonable, especially because the data are only being used to provide upper limits to our SED model fits in most cases.

B.2. Extended Sources

Table 8 shows the Spitzer-IRAC photometry values for all extended sources. We performed a color–color analysis similar to that in Figure 11 to determine that all sources are PAH contaminated. Thus, all flux values at 3.6, 5.8, and 8.0 μm are considered upper limits. The uncontaminated 4.5 μm flux values were used as nominal data points, and background subtraction was performed only for these data (see Table 8).

The Herschel-PACS photometry of extended sources can be found in Tables 9 and 10. As we already note from compact source photometry, there are certain areas covered by saturated pixels in some bands. For the extended sources where the area of saturated pixels was less than 10% of the photometric aperture area, we performed simple 2D Gaussian fitting of the sources to estimate flux values for each saturated pixel. If more than 10% of the area of an extended source is covered by saturated pixels, we did not derive a flux value for that band and therefore exclude those data from the SED fitting (Table 9). For regions that were resolved well enough at 70 and or 160 μm in the Herschel data, we found the determined best aperture for each source given its radial profile and derived flux measurements with background subtraction (Table 10) and used these values in the evolutionary analyses in Section 4.2.1. For unresolved sources, we used fixed apertures of $16''$ for 70 μm, $22.''5$ at 160 μm, $30''$ at 250 μm, $40''$ at 350 μm, and $57.''5$ at 500 μm.

Table 8
Spitzer-IRAC Observational Parameters of Major Extended Subregions in W49A

Source	R_{int} ($''$)	3.6 μm F_{int} (Jy)	4.5 μm[a] F_{int} (Jy)	4.5 μm[a] F_{int-bg} (Jy)	5.8 μm F_{int} (Jy)	8.0 μm F_{int} (Jy)
AA	15.0	0.151	0.196	0.093	1.41	4.34
BB	14.2	0.280	0.344	0.164	2.62	7.22
CC	14.5	0.773	0.893	0.644	3.79	10.7
DD	12.0	0.258	0.392	0.213	2.64	7.39
G	11.2	0.327	0.714	0.565	3.92	8.72
HH	12.0	0.233	0.355	0.111	2.59	7.19
II	12.3	0.150	0.225	0.107	2.19	6.00
JJ	21.5	1.019	1.51	0.570	9.62	31.2
L + M	11.9	0.317	0.540	0.237	3.88	10.9
LL	17.5	0.229	0.318	0.150	2.43	6.90
MM	21.5	0.522	0.779	0.359	5.25	15.4
O	13.1	0.584	0.842	0.393	5.11	14.6
R + Q	15.4	0.901	1.881	1.70	9.10	19.5
S	10.2	0.442	0.745	0.455	3.70	10.2
W49South	25.5	1.59	3.67	3.17	17.7	37.2

Note.
[a] For Spitzer-IRAC data, only fluxes at 4.5 μm are uncontaminated by PAH emission. Fluxes at all other wavelengths are used as upper limits and therefore do not have any background subtraction performed.

Table 9
Herschel-PACS Observational Parameters of Major Extended Subregions in W49A (No Background Subtraction)

Source	70 μm F_{int} (Jy)	160 μm F_{int} (Jy)	250 μm F_{int} (Jy)	350 μm F_{int} (Jy)	500 μm F_{int} (Jy)
CC	1018	1532	292[a]	229[a]	247[a]
DD	1453	1012	…	…	676[a]
G Region	16676[a]	10136[a]	…	…	812[a]
HH	834	1227	…	…	588[a]
II	1365	1471	…	…	545[a]
JJ	2103	1453	619	334	219
L + M Region	3968	3041[a]	…	…	762[a]
LL	1129	1037	244	142	97.5
MM	1029	698	275	131	98.4
O Region	3321	1236	…	532	355[a]
R + Q Region	1634	738	491	249	143[a]
S	1263	795	467	262[a]	200[a]
W49 South	5150	2836	1090[a]	336	188

Notes. Photometry values at 250 and 350 μm are not given for sources DD, G Region, HH, II, and L + M Region as more than 10% of the area within the source aperture are saturated pixels. The 250 μm value for the O Region is also not given for the same reason.
[a] These sources contain saturated pixels inside the photometry aperture covering less than 10% of the area. Simple 2D Gaussian fitting has been performed to estimate the flux values of the pixels.

Table 10
Herschel-PACS Observational Parameters of Major Extended Subregions in W49A (Background Subtracted)

Source	70 μm		160 μm	
	$R_{\rm int}$ ($''$)	$F_{\rm int\text{-}bg}$ (Jy)	$R_{\rm int}$ ($''$)	$F_{\rm int\text{-}bg}$ (Jy)
CC	19.2	501	27.0	581
DD	16.0	508	22.5	…
G Region	25.6	13596	27.0	7852
LL	16.0	768	22.5	757
O Region	16.0	1725	22.5	…
R + Q Region	16.0	1343	18.0	723
S	12.8	979	13.5	191
W49 South	22.4	4452	22.5	1689

ORCID iDs

James M. De Buizer https://orcid.org/0000-0001-7378-4430
Wanggi Lim https://orcid.org/0000-0003-4243-6809
Mengyao Liu https://orcid.org/0000-0001-6159-2394
Nicole Karnath https://orcid.org/0000-0003-3682-854X
James T. Radomski https://orcid.org/0000-0003-0740-2259

References

Alves, J., & Homeier, N. 2003, ApJL, 589, L45
Barbosa, C. L., Blum, R. D., Damineli, A., Conti, P. S., & Gusmão, D. M. 2016, ApJ, 825, 54
Becklin, E. E., Neugebauer, G., & Wynn-Williams, C. G. 1973, ApL, 13, 147
Bisbas, T. G., Tan, J. C., Csengeri, T., et al. 2018, MNRAS, 478, 54
Buckley, H. D., & Ward-Thompson, D. 1996, MNRAS, 281, 294
Clarke, M., Vacca, W. D., & Shuping, R. Y. 2015, in Proc. Conf. 24th ADASS, 495 (Calgary, Alberta: ASP), 355
Conti, P. S., & Blum, R. D. 2002, ApJ, 564, 827
Conti, P. S., & Crowther, P. A. 2004, MNRAS, 355, 899
De Buizer, J. M. 2006, ApJL, 642, L57
De Buizer, J. M., Liu, M., Tan, J. C., et al. 2017, ApJ, 843, 33
De Pree, C. G., Mehringer, D. M., & Goss, W. M. 1997, ApJ, 482, 307
De Pree, C. G., Wilner, D. J., Goss, W. M., et al. 2000, ApJ, 540, 308
De Pree, C. G., Wilner, D. J., Kristensen, L. E., et al. 2020, AJ, 160, 234
Dickel, H. R., & Goss, W. M. 1990, ApJ, 351, 189
Dreher, J. W., Johnston, K. J., Welch, W. J., et al. 1984, ApJ, 283, 632
Elia, D., Molinari, S., Schisano, E., et al. 2017, MNRAS, 471, 100
Garay, G., Brooks, K. J., Mardones, D., et al. 2003, ApJ, 587, 739
Gutermuth, R. A., Megeath, S. T., Myers, P. C., et al. 2009, ApJS, 184, 18
Herter, T. L., Vacca, W. D., Adams, J. D., et al. 2013, PASP, 125, 1393
Homeier, N. L., & Alves, J. 2005, A&A, 430, 481
Hunter, T. R., Brogan, C. L., MacLeod, G. C., et al. 2018, ApJ, 854, 170
Jackson, J. M., & Kraemer, K. E. 1994, ApJL, 429, L37
Kim, W.-J., Urquhart, J. S., Wyrowski, F., et al. 2018, A&A, 616, A107
Krumholz, M. R., & Tan, J. C. 2007, ApJ, 654, 304
Lada, C. J., & Lada, E. A. 2003, ARA&A, 41, 57
Lim, W., & De Buizer, J. M. 2019, ApJ, 873, 51
Lim, W., De Buizer, J. M., & Radomski, J. T. 2020, ApJ, 888, 98
Lim, W., Nakamura, F., Wu, B., et al. 2021, PASJ, 73, 239
Lim, W., Tan, J. C., Kainulainen, J., Ma, B., & Butler, M. J. 2016, ApJL, 829, L19
Lucy, L. B. 1974, AJ, 79, 745
Ma, B., Tan, J. C., & Barnes, P. J. 2013, ApJ, 779, 79
Mezger, P. G., Schraml, J., & Terzian, Y. 1967, ApJ, 150, 807
Moisés, A. P., Damineli, A., Figuerêdo, E., et al. 2011, MNRAS, 411, 705
Molinari, S., Schisano, E., Elia, D., et al. 2016, A&A, 591, 149
Mufson, S. L., & Liszt, H. S. 1977, ApJ, 212, 664
Peng, T.-C., Wyrowski, F., van der Tak, F. F. S., et al. 2010, A&A, 520, A84
Plume, R., Kaufman, M. J., Neufeld, D. A., et al. 2004, ApJ, 605, 247
Purser, S. J. D., Lumsden, S. L., Hoare, M. G., et al. 2016, MNRAS, 460, 1039
Richardson, W. H. 1972, JOSA, 62, 55
Rugel, M. R., Rahner, D., Beuther, H., et al. 2019, A&A, 622, 48
Samal, M. R., Zavagno, A., Deharveng, L., et al. 2014, A&A, 566, A122
Saral, G., Hora, J. L., Willis, S. E., et al. 2015, ApJ, 813, 25
Serabyn, E., Guesten, R., & Schulz, A. 1993, ApJ, 413, 571
Smith, L. F., Biermann, P., & Mezger, P. G. 1978, A&A, 66, 65
Smith, N., Jackson, J. M., Kraemer, K. E., et al. 2000, ApJ, 540, 316
Smith, N., Whitney, B. A., Conti, P. S., de Pree, C. G., & Jackson, J. M. 2009, MNRAS, 399, 952
Umemoto, T., Minamidani, T., Kuno, N., et al. 2017, PASJ, 69, 78
Urquhart, J. S., Thompson, M. A., Moore, T. J. T., et al. 2013, MNRAS, 435, 400
Wang, L.-L., Luo, A.-L., Hou, W., et al. 2018, PASP, 130, 430
Ward-Thompson, D., & Robson, E. I. 1990, MNRAS, 244, 458
Webster, W. J., Altenhoff, W. J., & Wink, J. E. 1971, AJ, 76, 677
Welch, W. J., Dreher, J. W., Jackson, J. M., et al. 1987, Sci, 238, 1550
Westbrook, W. E., Werner, M. W., Elias, J. H., et al. 1976, ApJ, 209, 94
Westerhout, G. 1958, BAN, 14, 215
Young, E. T., Becklin, E. E., Marcum, P. M., et al. 2012, ApJL, 749, L17
Zhang, B., Reid, M. J., Menten, K. M., et al. 2013, ApJ, 775, 79